CZECH TECHNICAL UNIVERSITY IN PRAGUE

FACULTY OF MECHANICAL ENGINEERING

Department of Aerospace Engineering

MASTER THESIS

Effect of Deformation of the Aircraft Model on the Aerodynamic Characteristics

Supervisor of the Master Thesis: Ing. Tomáš Čenský, Ph.D.

Prague, 2018

Author: Andrii Tafiichuk

ZADÁNÍ DIPLOMOVÉ PRÁCE

I. OSOBNÍ A STUDIJNÍ ÚDAJE

Příjmení: **Tafiichuk** Jméno: **Andrii** Osobní číslo: **411231**

Fakulta/ústav: **Fakulta strojní**

Zadávající katedra/ústav: **Ústav letadlové techniky**

Studijní program: **Letectví a kosmonautika**

Studijní obor: **Letadlová a kosmická technika**

II. ÚDAJE K DIPLOMOVÉ PRÁCI

Název diplomové práce:

Vliv deformace modelu dopravního letounu na aerodynamické charakteristiky

Název diplomové práce anglicky:

Effect of Deformation of the Aircraft Model on the Aerodynamic Characteristics

Pokyny pro vypracování:

1. Rešerše aktuálního stavu problematiky deformace tunelového modelu.
2. Analýza deformací tunelového modelu vlivem aerodynamických sil.
3. Návrh geometrických modelů a objemových sítí pro CFD výpočet.
4. Analýza vlivu sítě a numerického modelu na aerodynamické vlastnosti.
5. Zhodnocení vlivu deformací tunelového modelu na aerodynamické charakteristiky.

Seznam doporučené literatury:

Dle pokynů vedoucího DP

Jméno a pracoviště vedoucí(ho) diplomové práce:

Ing. Tomáš Čenský, Ph.D., ústav letadlové techniky FS

Jméno a pracoviště druhé(ho) vedoucí(ho) nebo konzultanta(ky) diplomové práce:

Datum zadání diplomové práce: **30.04.2018** Termín odevzdání diplomové práce: **13.08.2018**

Platnost zadání diplomové práce: _____

Ing. Tomáš Čenský, Ph.D.	Ing. Robert Theiner, Ph.D.	prof. Ing. Michael Valášek, DrSc.
podpis vedoucí(ho) práce	podpis vedoucí(ho) ústavu/katedry	podpis děkana(ky)

III. PŘEVZETÍ ZADÁNÍ

Diplomant bere na vědomí, že je povinen vypracovat diplomovou práci samostatně, bez cizí pomoci, s výjimkou poskytnutých konzultací. Seznam použité literatury, jiných pramenů a jmen konzultantů je třeba uvést v diplomové práci.

26.04.2018
Datum převzetí zadání

Podpis studenta

At this point I wish to thank the Department of Aerospace Engineering, Czech Technical University in Prague, VZLU Technologies, A.s. for providing the facilities to carry out this master thesis work. My sincere thanks to Ing. Tomáš Čenský, Ph.D. and Ing. Petr Vrchota, Ph.D. for professional guidance and valuable advices during developing of this thesis. Last but not least I would like to thank my parents for their support during my study and my friends who were supporting me regarding this work.

Solemn declaration

I declare that I carried out this bachelor thesis independently, and only with the cited sources, literature and other professional sources.

In Prague, 22.08.2018 signature 

Anotace

Jméno Autora: Andrii Tafiichuk

Název diplomové práce: Vliv deformace modelu dopravního letounu na aerodynamické charakteristiky

Název diplomové práce anglicky: Effect of Deformation of the Aircraft Model on the Aerodynamic Characteristics

Rok: 2018

Studijní program: Letectví a kosmonautika

Studijní obor: Letadlová a kosmická technika

Ústav: Ústav letadlové techniky

Vedoucí diplomové práce: Ing. Tomáš Čenský, Ph.D.

Bibliografické údaje: počet stran: 62
počet obrázků: 42
počet tabulek: 15
počet příloh: 6

Klíčová slova: Model letadla, deformace, aerodynamické charakteristiky, vliv deformace, NASA CRM, aerodynamika, simulace proudění, model turbulence, ANSYS Fluent, počítačová dynamika tekutin, CFD, návrh výpočetních sítí, porovnání numerických a experimentálních dat.

Keywords: Aircraft model, deformation, aerodynamic characteristics, effect of deformation, NASA CRM, aerodynamics, flow simulation, turbulence model, ANSYS Fluent, computational fluid dynamics, CFD, mesh design, comparison of numerical and experimental data.

Abstrakt: Během testování v aerodynamickém tunelu je model letadla vystaven deformacím způsobeným aerodynamickými silami. Tyto deformace ovlivňují aerodynamické vlastnosti modelu letadla. Tato práce se zaměřuje na zkoumání vlivu deformace na aerodynamické charakteristiky pro model letadla NASA Common Research Model (CRM). Cílem je analyzovat elastický a tuhý případ NASA CRM, porovnat jejich aerodynamické charakteristiky, tj. koeficienty vztlaku, odporu a klopivého momentu, rozložení tlaků a poskytnout vyhodnocení vlivu deformací tunelového modelu na jeho aerodynamické charakteristiky. Analýza se provádí na základě CFD simulace deformovaného modelu a modelu bez deformace. Pro tento účel je vybrán software ANSYS Fluent.

Abstract: During wind tunnel testing the aircraft model is subjected to the deformations due to aerodynamic forces. These deformations influence the aerodynamic characteristics of the aircraft model. This work focuses on investigation of the effect of deformation on the aerodynamic characteristics of the NASA Common Research Model (CRM) aircraft model. The goal is to analyze elastic and rigid case of NASA CRM, compare their aerodynamic characteristics i.e. lift, drag and pitching moment coefficients, pressure distributions, and to give an evaluation of the impact of tunnel model deformations on its aerodynamic characteristics. The analysis is performed based on the CFD simulation of the un-deformed and deformed aircraft model. For this purpose, ANSYS Fluent software package is chosen.

List of abbreviations

AIAA – American Institute of. Aeronautics and Astronautics

AOA, α – Angle of Attack

CAD – Computer-aided design

CFD – Computational Fluid Dynamics

CRM – Common Research Model

DES – Detached Eddy Simulation

DNS – Direct Numerical Simulation

FEM – Finite Element Method

Fluent – ANSYS Fluent CFD software

FSI – Fluid Structure Interaction

HTP – horizontal tail plane

LES – Large Eddy Simulation

M – Mach number

MAC – Mean aerodynamic chord

NASA – National Aeronautics and Space Administration

NTF – NASA Langley National Transonic Facility Wind Tunnel

NX – Siemens NX CAD software

PIV – Particle Image Velocimetry

RANS – Reynolds Averaged Navier–Stokes equations

Re – Reynolds number

SST model – Shear-Stress Transport k-ω turbulence model

ρ – fluid density

k – turbulent kinetic energy

ω – specific rate of dissipation

∇ – divergence vector operator

C_D – drag coefficient

C_L – lift coefficient

C_M – pitching moment coefficient

C_P – pressure coefficient

M – mass

u, V – velocity of the fluid

y^+ – dimensionless wall distance

Table of Contents

4. Computation & Results

1. Introduction

1.1 Problem Description

The aim of this work is to give an investigation of the influence of deformation on the aerodynamic characteristics of the aircraft model. The candidate vehicle is NASA Common Research Model (CRM) [1] which is contemporary supercritical transonic wing and a fuselage that is representative of a widebody commercial transport aircraft. It is designed for a cruise Mach number of $M\infty = 0.85$ and a corresponding design lift coefficient of $CL= 0.5$.

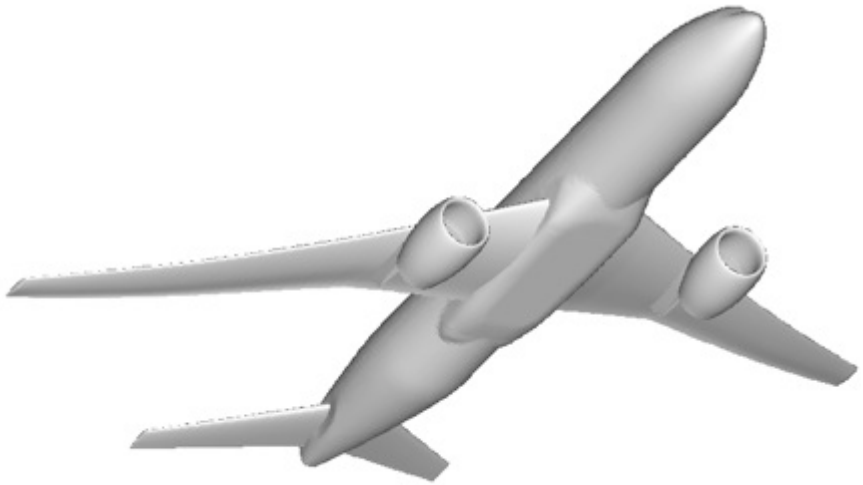

Figure 1-1. NASA CRM Wing/Body/Nacelle/Pylon/Horizontal-Tail Configuration [1]

The Common Research Model was developed as result of several parties asking NASA to help develop experimental databases for the purpose of validating specific applications of Computational Fluid Dynamics (CFD) [2].

The CRM is represented in various configurations including several settings of Horizontal Tail Plane (HTP), nacelle and pylon. It is equipped with pressure taps to measure the pressure distributions.

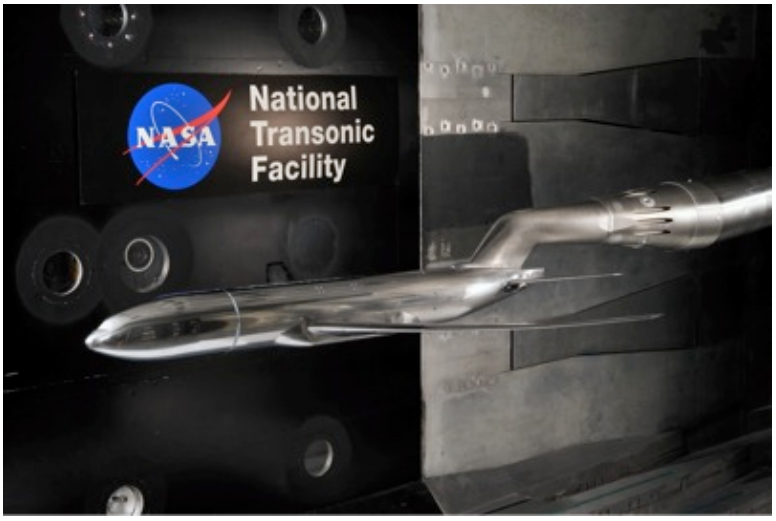

Figure 1-2. NASA CRM at NASA National Transonic Facility Wind Tunnel [1]

1.2 Objectives

At present, wind tunnel tests are still used throughout the design process both as a means of assessing the current level of aircraft performance and in order to calibrate the CFD codes being used. To achieve the reliable aerodynamic comparison between experimental and CFD data the deformation effects must be considered.

The primary purpose of this work is and investigation of the different aerodynamic characteristics e.g. the relationship between lift coefficients and drag coefficients with angle of attacks, pressure distributions along the chords of wing and comparison of those between rigid and elastic case of NASA CRM model.

Considering all above, the objectives of the work are formulated as follows:

- to perform analysis of wind tunnel model deformation due to aerodynamic forces.
- to develop computational grids and calculation procedure for CFD simulation.
- to check the grid and numerical model influence on aerodynamic properties during CFD simulation.
- to compare both deformed and non-deformed cases of NASA CRM and to give an evaluation of the impact of tunnel model deformations on aerodynamic characteristics.

2. Theoretical Background

2.1 Effect of Deformation

The aircraft performance is strongly bounded to its aerodynamic properties. During development stage of an aircraft a considerable effort is typically spent on the evaluation and improvement of the aerodynamic design.

For many engineering applications the rigid geometry assumption holds. As for Aerospace Engineering, those assumptions can't be taken, aeroelastic effects become important to consider, as they have significant influence on aircraft's design and weight of the structure, and its aerodynamic performance.

As for the model of aircraft, during wind tunnel testing it is subjected to the deformations due to aerodynamic forces (Fig 2-1). Generally, it is seen as a crucial effect on the aerodynamic characteristics in cases where the ratio of dynamic pressure over Young modulus is high. These cases correspond to the wind tunnel measurements with realistic fight conditions [3].

This aerodynamic effect was ignored for a long time. Perhaps the reason is that deformation level was unknown and barely measurable because of the lack of an appropriate method [4]. Deformation of the model of the aircraft was considered a major source of error only in the beginning of 2000s [5].

Since the wing of the airplane is the part that generates the most of the aerodynamic force, this and its slender shape results in the deformation, that is significantly changes the

flow field and therefore can have big influence on the aerodynamic properties of aircraft. Other parts have very small influence on the aerodynamic characteristics of the aircraft model [5]. For the purposes of this work they can be neglected. Also, the wing aerodynamic properties are greatly sensitive to its shape, especially in transonic flow [6]. Understanding these effects can improve the prediction of aircraft flight dynamics and improve aerodynamic design.

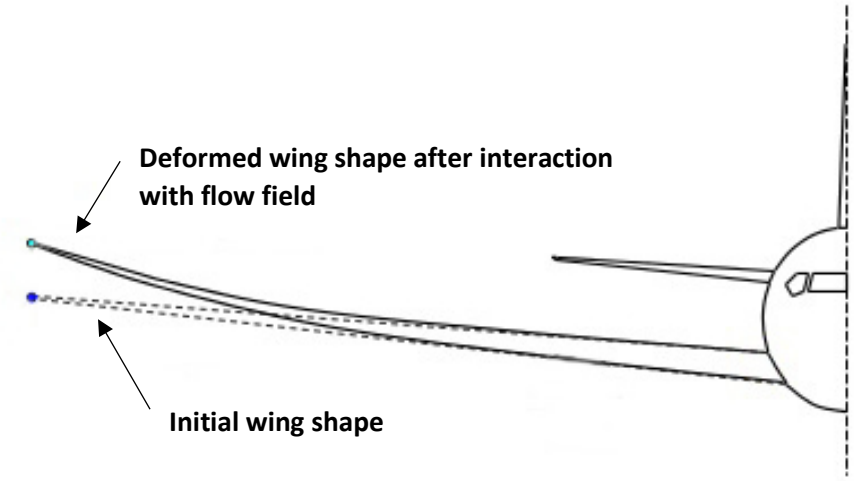

Figure 2-1. Deformation of the aircraft model

In present time the deformation of the wing is being measured in most of the wind tunnel tests using optical techniques [5]. Therefore, determination of the deformed wing shape, which is available from wind tunnel measurements, is not the case of this study. This work focuses on investigation of the effect of wing deformation on the aerodynamic characteristics of the aircraft.

Elastic effects of model in wind tunnel has to be considered in Computational Fluid Dynamics simulations for the sake of improving their accuracy. There are various methods how to include the model deformation in the CFD simulation. One of the methods is the deformation of the CFD model according to the measured deformation of the wind tunnel model, where the surface geometry is manually shaped to match the measured wing deformation for particular angle of attack (AoA). Another method is a coupling between CFD and Finite Element Method (FEM) solvers, which is known as Fluid-Structure Interaction (FSI) [7].

2.2 Computational Fluid Dynamics

Studies of aerodynamic characteristics of aircraft, are based on theoretical and experimental methods. The main instrument of experimental method is a wind tunnel testing, where most of the research is currently being conducted. However, as technology becomes more sophisticated, the trends in the growth of the cost of such studies arise, as well as the insufficiency of obtained information because of their fundamental limitations. This serves as major push factor in the development of the solutions based on CFD.

2.2.1 Brief Overview

Computational fluid dynamics codes have been extensively developed during the last decades and have enabled notable improvements in aerodynamic design [8]. As for today, CFD models with a wide range of computational complexity, accuracy are available, and widely used for design purposes. Still, it appears that further developments in terms of computational efficiency, physics modeling and reliability could provide significant value to aircraft design and supposedly enable time and cost savings as well as improved design solutions [8].

Evolution of CFD has begun with the modeling of two-dimensional potential flows in the 1970s and reached till application of programs numerically solving the three-dimensional Navier-Stokes equations with more advanced models of turbulence (LES – Large Eddy Simulation, DES – Detached Eddy Simulation) for complex geometries, which led to drastic efficiency improvement (Fig. 2-2). Between them is a period of time when different equations for the description of complex turbulent flows were introduced in industry. It can be noted that the three-dimensional inviscid Euler equations were introduced in the mid-1980s, and the full three-dimensional Navier-Stokes equations modeling turbulent flows started to be used in late 1990s [11]. This development was associated with both the growing performance of computing systems, and with the improvement of algorithms and techniques in CFD analysis.

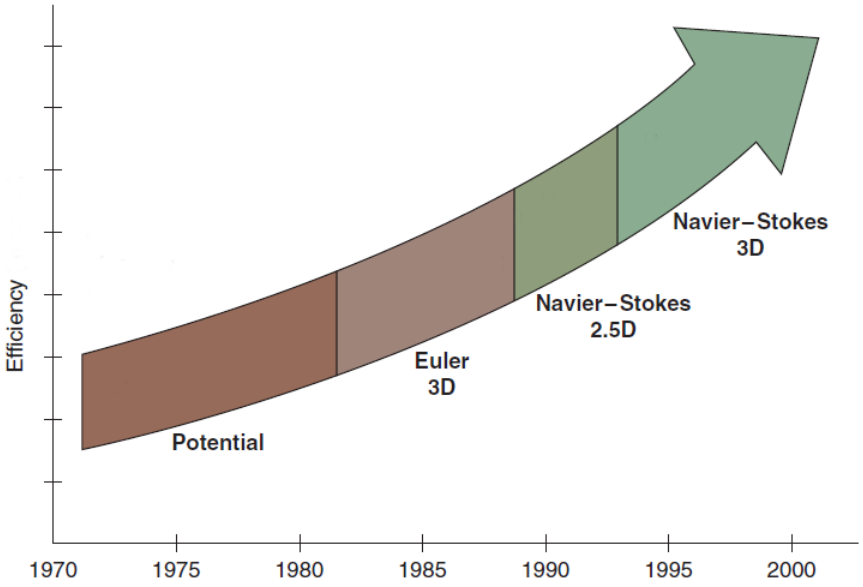

Figure 2-2.. Evolution of CFD [11]

At present, in the practice of scientific and applied research, CFD application packages are increasingly being used. However, their practical use is associated with a number of problems that researcher is being forced to solve in one way or another. These include the choice of the calculated area and the construction of an appropriate grid, the assignment of adequate boundary conditions, the use of an appropriate model of turbulence, and so on. In other words, the application of the package requires its thorough testing in the solved class of tasks [8].

2.2.2 CFD vs Experiment

CFD has many advantages over a full experiment:

- Significant reduction in design time and reduced production costs
- The ability to study complex systems where it is difficult or impossible to conduct an experiment
- The ability to study the behavior of systems, technical devices operations beyond their normal functioning (for safety research)
- The possibility of visualizing vortex structures, determining the detachment of the boundary layer, constructing spatial streamlines, etc. Numerical CFD analysis gives an almost unlimited amount of data
- Better understanding of physical, aerodynamic and thermal processes

Carrying out the experiment requires very expensive equipment (e.g wind tunnels), as well as equipment for measuring aerodynamic forces, flow visualization (PIV, fluorescent pressure transducers, etc.) [9].

On the contrary, CFD allows you to put a virtual numerical experiment in a fairly short time, while significantly saving financial resources. It gives enables to solve the flows that can be difficult, expensive, impossible to study using experimental approach.

Experimental approach (Wind Tunnel)	Numerical approach (CFD simulation)
• description of flow using measurements • for one quantity at a time • for a size of laboratory-scale model • at a limited number of points and time instants • for a limited range of problems and operating conditions • expensive • sequential • sources of errors: measurement errors, flow disturbances by the probes	• prediction of flow using numerical calculations • for all desired quantities • for a size of actual flow domain • with high resolution in space and time • for virtually any problem and realistic operating conditions • cheap(er) • fast(er) • parallel • sources of errors: modeling techniques, implementation techniques

Table 2-1. Comparison between experimental and numerical approach

Fluid dynamics suggests several types of equations to be used in numerical calculations. The difference between them is determined by the accepted restrictions and correspondingly by more or less great correspondence to the real-life flow around the object. The most complete information about the motion of fluid and the most accurate results can be obtained by numerical methods based on solving the Navier-Stokes equations describing the viscous flow around the object [6]. More information about it will be presented in next section.

Graphical representation of the whole process of Computational Fluid Dynamics is showed in Figure 2-3.

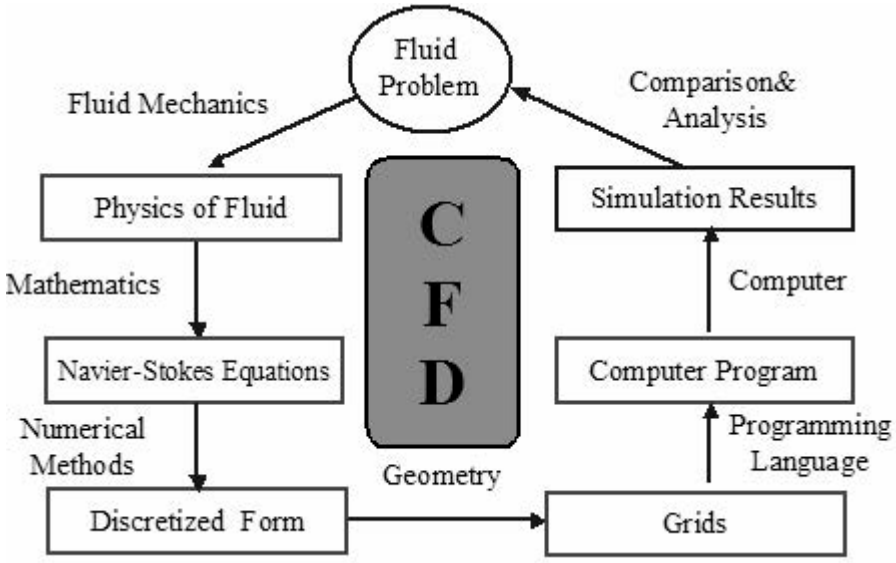

Figure 2-3. Process of CFD

Setting up the such system and solving it (which is a matrix inversion problem) [9] involves a very large number of repetitive calculations, the task which is mostly suitable for computers.

2.3 Governing Equations of Fluid Dynamics

The governing equations the fluid dynamics are based on fundamental physics principles:

– change of mass = 0
– change of momentum = force × time
– change of energy = work + heat

Those principles represent 3 conservation laws: conservation of mass, momentum, and energy. For example, for the conservation of mass it states that the mass change in an object is decided by the input and output [10].

$$\frac{dM}{dt} = \dot{m_{in}} - \dot{m_{out}} \qquad \text{(eq. 2-1)}$$

if $\dot{m_{in}} - \dot{m_{out}} = 0$, then

$$\frac{dM}{dt} = 0 \quad \rightarrow \quad M = const \qquad \text{(eq. 2-2)}$$

By applying mass, momentum and energy conservation, it is possible to derive the continuity equation, momentum equation and energy equation as follows.

Continuity equation:

$$\frac{d\rho}{dt} + \nabla \cdot (\rho \vec{u}) = 0 \qquad \text{(eq. 2-3)}$$

Equation (2-3) is the unsteady, three-dimensional continuity equation or mass conservation equation at a point in a compressible fluid. Where $\vec{u}$ represents velocity vector, ρ represents the density of the fluid, $\nabla \cdot$ represents divergence vector operator. The first term of

the equation is the rate of change of density with respect to time and the second term is net flow of mass out of element boundaries [10].

Momentum equation:

$$\frac{d(\rho\vec{u})}{dt} + \nabla \cdot (\rho\vec{u} \times \vec{u}) = -\nabla p + \nabla \cdot \bar{\bar{\tau}} + \rho\vec{f} \qquad \text{(eq. 2-4)}$$

Equation (2-4) represents Newton's second law which states that the rate of change of momentum of a fluid particle equals to the sum of the forces acting on a particle. The forces acting on a body are a combination of both surface and body forces [9]. Where p represents pressure, $\vec{f}$ represents body force per unit mass and $\bar{\bar{\tau}}$ is viscous stress tensor. If the weight of the fluid is the only body force then $\vec{f}$ can be replaced with the gravitational acceleration vector $\vec{g}$. As for stress tensor, if the fluid is Newtonian fluid then viscous stresses only depend on the velocity gradient and the dependency is linear [10].

Energy equation:

$$\frac{d(\rho i)}{dt} + \nabla \cdot (\rho i\vec{u}) = -p\nabla \cdot \vec{u} + \nabla \cdot (k\,\nabla T) + \Phi \qquad \text{(eq. 2-5)}$$

Where i is the specific enthalpy which is related to specific internal energy as $i = e + p/\rho$. T is the absolute temperature and Φ is the dissipation function representing the work done against viscous forces, which is irreversibly converted into internal energy.

This system of equations above is often referred to as the compressible Navier-Stokes equations. In general, all three equations need to be solved simultaneously, which names them coupled system of equations [9]. There are actually some other equation that are required to solve this system.

$$p = \rho RT \qquad \text{(eq. 2-6)}$$

An equation (2-) of state of ideal gas relates the pressure, temperature, and density of the gas, where R is universal gas constant. Also, all of the terms of the stress tensor need to be specified in order to solve such system. In CFD the stress tensor terms are often approximated by a turbulence model [12].

2.4 Discretization

The basic step of CFD is dividing the computational domain (the geometry of the region of interest) into the number of smaller regions (control volumes or cells). The collection of these cells is called a grid or a mesh. In the broadest sense, CFD strategy implies replacing the continuous problem domain with a discrete domain by use of grid [9]. In the continuous domain, each flow variable is defined at every point in the domain. For instance, the pressure p in the continuous 1-D domain would be represented as:

$$p = p(x), \qquad 0 < x < 1$$

In the discrete domain, on the other hand, each flow variable would be defined only at the grid points [9]. So, for example, in the discrete domain the pressure is defined only at the N grid points, as:

$$p_i = p(x_i), \qquad i = 1, 2, \ldots, N$$

Figure 2-4 gives graphical representation of this formulation.

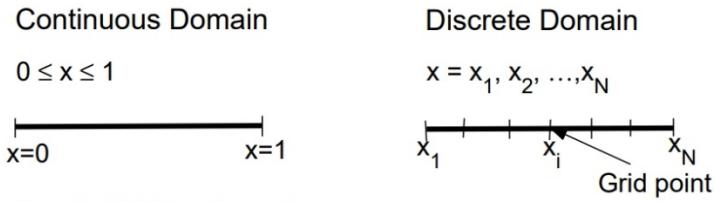

Figure 2-4. Continuous and Discrete Domain representation

CFD solution implies direct solving of the corresponding flow variables only at the grid points. By interpolating the values at the grid points, the values at other locations are found.

The Navier-Stokes equations general conservation equations. Those governing equations and boundary conditions are defined as continuous variables p, V, etc. In CFD, in order to solve such system, this is approximated into the discrete domain in terms of the discrete variables p_i , V_i, etc. Thus, the discrete system is a large set of coupled, algebraic equations in the discrete variables. This process is called discretization. There are couple of discretization methods such as finite difference, finite element and finite volume methods [10]. A brief overview of finite volume method is introduced in next section.

2.5 Finite Volume Method

The finite volume method is one of the numerical approaches applied in CFD codes to solve the governing equations of the fluid. After the computational domain has been divided into the number of smaller regions i.e. grid, the calculated scalar values are stored at the center of the control volumes. The finite volume technique is used to convert the general conservation (transport) equations of mass, momentum, energy into a system of algebraic equations and with use of different iterative methods to solve such system.

In the finite volume method, the integral form of the conservation equations is applied to the control volume defined by a cell to get the discrete equations for the cell [9]. As a simple example, consider one rectangular cell of the 2-D grid (Figure 2-5).

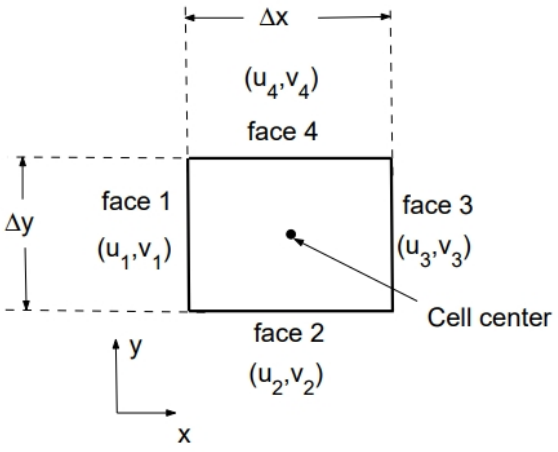

Figure 2-5. Typical rectangular cell of the grid

The integral form of the continuity equation for steady, incompressible flow is:

$$\iint_S \vec{u} \cdot \hat{n}\, dS = 0 \qquad \text{(eq. 2-7)}$$

where the integration is over the surface S of the control volume and $\hat{n}$ is the outward normal vector to the surface. Physically speaking, equation (2-7) means that the net volume flow into the control volume is zero.

Now, the velocity at face i would to be $\vec{u} = u_i\,\hat{i} + v_i\,\hat{j}$. Application of the mass conservation equation (2-6) to the control volume which is defined by the cell gives:

$$-u_1\Delta y - v_2\Delta x - u_3\Delta y - v_4\Delta x = 0 \qquad \text{(eq. 2-8)}$$

Equation (2-9) is the discrete form of continuity equation for the cell. It is equivalent to summing up the net mass flow into the control volume and setting it to zero. Thus, it ensures that the net mass flow into the cell is zero i.e. that mass is conserved for the cell [10].

The following are the key steps for finding the solution of the transport equation of a physical quantity [9]:

- Dividing the geometry in to smaller regions (control volumes) using a computational mesh.
- Integrating the governing equations over all the control volumes of the domain.
- Discretization process i.e. converting the resulting integral equations into a system of algebraic equations.
- Finding a solution to the system of algebraic equations using iterative method.

As for a finite difference or finite element approach for discretized Navier-Stokes equations, there is a need to manually control the conservation of mass, momentum and energy. With a finite volume method, on the other hand, it is easy to find out that, if the Navier-Stokes equations are satisfied in every control volume, then it would be automatically satisfied for the whole domain. That is the reason why finite volume method is preferred in CFD [9].

2.6 Turbulent Flow

All flows encountered in engineering practice, simple ones two-dimensional, and more complicated three-dimensional ones, become unstable above a certain critical Reynolds number (Re). The Reynolds number (eq. 2-10) gives prediction of flow patterns in different fluid flow situations. It is also being used for the scaling of similar but different-sized flow problems, such as an aircraft model in a wind tunnel and the full-size aircraft [10].

$$Re = \frac{inertia\ forces}{viscous\ foces} = \frac{\rho\, V\, L}{\mu} \qquad \text{(eq. 2-10)}$$

where V is free steam velocity, L is characteristic length, for example Mean Aerodynamic Chord for the wing; and μ is dynamic viscosity of the fluid.

For a low Reynolds number, the flow tends to be smooth, dominated by laminar (sheet-like) layers. For a high Reynolds number, a complicated series of events takes place which leads formation of the differences in the fluid's speed and direction, which may sometimes intersect or even move counter to the overall direction of the flow (eddy currents) [10]. As a result, the flow behavior is random and chaotic. This regime is called turbulent flow. According to Versteeg, H. [10], for external flow problem the critical Re, above which transition from laminar to turbulent flow happens, has a value around $5 \cdot 10^5$ [10]. A point velocity measurement is shown on Figure 2-6.

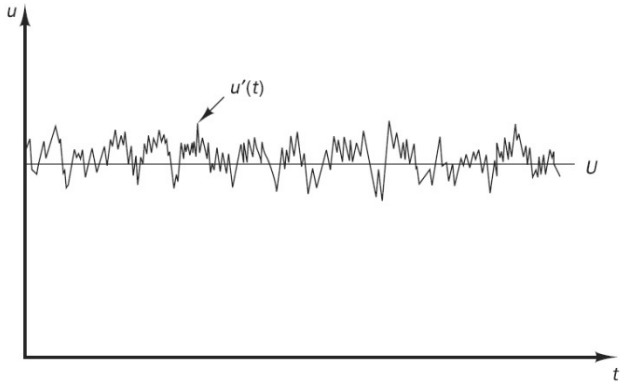

Figure 2-6. Velocity fluctuation for a turbulent flow [10]

The random nature of the turbulent flow eliminates the economical description of the motion of all fluid particles. To model the turbulent flow, the following approach is used: the velocity decomposes into a stable average value U with the fluctuating component u′(t) superimposed on it, which gives: u(t) = U + u′(t) (Figure 2-6). This process is called Reynolds decomposition [13]. A turbulent flow can now be represented in terms of the average values of flow properties (U, P etc.) and some statistical properties of their fluctuations (u′, p′ etc.) [10].

2.7 Turbulence modelling

Even though Navier-Stokes equations are capable of evaluating the solution by taking into consideration the turbulence effect, this needs huge amount of computational resources to simulate fluctuations in such small scales. This type of approach is called as Direct Numerical Simulation (DNS) [14]. As an alternative there exist methods, which use the turbulence models in order to simulate the effect of turbulence, such as The Reynolds Averaged Navier-Stokes simulation (RANS) and Large Eddy Simulation (LES). Such methods use its own kind of Navier-Stokes equation to simulate the turbulent flow by means of turbulence model [14]. In this work, RANS is being used for modelling to the effects of turbulence of the flow, thus a brief overview of RANS is presented in section 2.7.1.

In general, the turbulent flow is affected by the presence of walls. In the region near the wall, the solution variables have large gradients [13]. Therefore, an accurate representation of the flow in this region can give realistic solution. The most commonly used approach for modeling the wall bounded turbulent flow implies the use of the set of semi-empirical formulas – “wall functions”. Wall function is used as a bridge of the viscosity-affected region

between the wall and fully turbulent region of the flow. Different wall functions are explained in [13].

2.7.1 Reynolds Averaged Navier Stokes Simulation (RANS)

By substituting the flow variables of governing equations in this form will result in Reynolds Averaged Navier-Stokes equations. The decomposition of flow variables results in appearance of additional term in the equations, called Reynolds stress term, which is unknown [14]. The main motivation of RANS approach is to model the Reynolds stresses.

Boussinesq hypothesis relates the Reynolds stresses to the average velocity gradients [13]. It can be written in Cartesian coordinate system as:

$$-\rho u_i' u_j' = \mu_t \cdot \left(\frac{\partial u_i}{\partial x_j} + \frac{\partial u_j}{\partial x_i}\right) - \frac{2}{3}\left(\rho k + \mu_t \frac{\partial u_k}{\partial x_k}\right)\delta_{ij} \qquad \text{(eq. 2-11)}$$

where δ_{ij} is Kronecker delta, μ_t is the turbulent viscosity, k is the kinetic energy. This hypothesis is used in turbulence models such as Spalart-Allmaras model, k-ε models and the k-ω models [13]. An overview of couple of RANS turbulence models is presented below.

2.7.2 k- ε model

There are a lot of models that can represent turbulence effect of the flow. By far, the most popular two-equation model is k-ε model [15]. This model was designed by Launder and Spalding in 1974 [15]. It has historically been very popular for industrial applications due to its robustness, low computational power requirements and sufficient precision for a wide range of types of turbulent flow.

This is a semi-empirical model and the derived model equations mostly rely on empirics and consideration. The main assumption is that the flow is fully turbulent and the effect of molecular viscosity is negligible [15]. However, this model has poor performance in the situations where the flow experiences large curvature, vortices, rotation, flow separation and lower Reynolds numbers. That's why, over time, other modifications of original k-epsilon model have been developed, such as RNG and Realizable which take advantage of its benefits and try to overcome its drawbacks [15].

The Realizable k-ε model brings a significant improvement over the standard k-ε model for flows with large curvature, vortices and rotation. Similarly to the standard k-ε model, the Realizable k- ε model solves two additional transport equations: one for turbulent kinetic energy (k) (eq. 2-12), one for rate of dissipation (ε) (eq. 2-13)

$$\frac{\partial}{\partial t}(\rho k) + \frac{\partial}{\partial x_j}(\rho k u_j) = \frac{\partial}{\partial x_j}\left(\left(\mu + \frac{\mu_t}{\sigma_k}\right)\frac{\partial k}{\partial x_j}\right) + G_k + G_b - \rho\varepsilon - Y_M + S_k\,, \qquad \text{(eq. 2-12)}$$

$$\frac{\partial}{\partial t}(\rho \varepsilon) + \frac{\partial}{\partial x_j}(\rho \varepsilon u_j) = \frac{\partial}{\partial x_j}\left(\left(\mu + \frac{\mu_t}{\sigma_k}\right)\frac{\partial \omega}{\partial x_j}\right) + \rho C_1 S\varepsilon - \rho C_2 \frac{\varepsilon^2}{k+\sqrt{\nu\varepsilon}} + \rho C_{1\varepsilon}\frac{\varepsilon}{k} C_{3\varepsilon} G_b + S_\varepsilon\,, \qquad \text{(eq. 2-13)}$$

In the equations above G_k is generation of turbulence kinetic energy due to average velocity gradients, G_b is of turbulence kinetic energy due to the lift, μ_t is turbulent viscosity, Y_M represents contribution to the total dissipation from fluctuating dilatations under compressible turbulent flow. σ_k and σ_ε are the constants: turbulent Prandtl numbers for of k and ε respectively. $C_{1\varepsilon}$ and C_2 are constants of the model as well, S_k and S_ε are the optional sources in the model [15].

Equations (2-12) and (2-13) are conservation equations for k and ε respectively. The left-hand side of equations represents storage and convection. This is balanced on the right-hand side by diffusion, source terms due to turbulence production (source) and turbulence dissipation (sink).

2.7.3 k-ω model

One of the models that is commonly used in aerospace engineering problems k-ω model. It was first developed by of Kolmogorov (1942), then several different and improved versions of Kolmogrov's model have been proposed, including those of: Wilcox (1988, 2008), Speziale et al (1990) and Menter (1992) [15]. I this section a brief description of Wilcox's standard k-ω model is given.

In comparison with k-ε model, the k-ω model is far more capable of producing accurate results in the flows that exhibit strong curvature and separated flows. Another advantage of the model is that equations of the model do not contain terms which are undefined at the wall, i.e. they can be integrated to the wall without using wall functions [13]. This model is accurate for a wide range of boundary layer flows with adverse pressure gradients.

This model, like k-epsilon model, solves for two variables, these are the turbulent kinetic energy (k) and the specific rate of dissipation of kinetic energy (ω). This model includes a low-Reynolds-number extension for near-wall turbulence [15]. The governing equations are represented below.

$$\frac{\partial}{\partial t}(\rho k) + \frac{\partial}{\partial x_i}(\rho k u_i) = \frac{\partial}{\partial x_j}\left(\Gamma_k \frac{\partial k}{\partial x_j}\right) + G_k - Y_k + S_k \qquad \text{(eq. 2-13)}$$

$$\frac{\partial}{\partial t}(\rho \omega) + \frac{\partial}{\partial x_i}(\rho \omega u_i) = \frac{\partial}{\partial x_j}\left(\Gamma_\omega \frac{\partial \omega}{\partial x_j}\right) + G_\omega - Y_\omega + S_\omega \qquad \text{(eq. 2-14)}$$

where G_k is generation of turbulence kinetic energy due to average velocity gradients, G_ω is the generation of specific dissipation rate, Γ_k is effective diffusivity of k, Γ_ω is effective diffusivity of ω. Y_k and Y_ω are the dissipation due to turbulence of k and ω respectively, S_k and S_ω are the optional sources in the model.

This model achieves better stability than the k-ε model, especially near the walls and it tends to produce converged solutions more rapidly than the k-ε models. However, the main weakness of this model is that unlike the k-ε model, is its sensitivity to the solving the values k and ω in the free flow outside the shear layers [15]. The model is relatively accurate near the wall and its accuracy decreases with distance from the wall. It can be said that its accuracy is opposite to the accuracy of the k-ε model. Therefore, modified variants of k-omega model exist which remove this sensitivity, such as Shear Stress Transport k-ω model.

2.7.4 SST k-ω model

The Shear-Stress Transport (SST) k–ω model was developed by Menter (1994) [13]. The model gradually transitions from the standard k–ω model near the wall to a high Reynolds number version of the k–ε model in the outer portion of the boundary layer. Thus, the model performs well up to the wall and lacks the common k-ω problem such as sensitivity to the inlet free-stream turbulence properties [15].

The SST k-ω model, like standard k-ω model, is two-equation turbulence model, which holds two additional transport equations: one for turbulent kinetic energy (k) (eq. 2-15), one for specific rate of dissipation (ω) (eq. 2-16) which both are required to be solved and the turbulent viscosity (μ_t) which is represented as a function of both k and ω [13].

$$\frac{\partial}{\partial t}(\rho k) + \frac{\partial}{\partial x_i}(\rho k u_i) = \frac{\partial}{\partial x_j}\left(\Gamma_k \frac{\partial k}{\partial x_j}\right) + \tilde{G}_k - Y_k + S_k \qquad \text{(eq. 2-15)}$$

$$\frac{\partial}{\partial t}(\rho \omega) + \frac{\partial}{\partial x_i}(\rho \omega u_i) = \frac{\partial}{\partial x_j}\left(\Gamma_\omega \frac{\partial \omega}{\partial x_j}\right) + G_\omega - Y_\omega + D_\omega + S_\omega \qquad \text{(eq. 2-16)}$$

where $\tilde{G}_k$ is generation of turbulence kinetic energy due to average velocity gradients calculated from G_k and G_ω is the generation of specific dissipation rate. Γ_k is effective diffusivity of k, Γ_ω is effective diffusivity of ω. Y_k and Y_ω are the dissipation due to turbulence of k and ω respectively. D_ω is the term of cross-diffusion, S_k and S_ω are the optional sources in the model.

The advantage of the SST model in comparison with the k-ω standard model is better suitability for unfavorable pressure gradients and flow separation, which are important for a drag analysis [13].

2.7.5 Transition model: K-kl-ω

Transition models are used to predict the change from laminar and turbulence flows in fluids and their respective effects on the overall solution. From the physical perspective, initially a laminar boundary layer develops in the flow. But then, due to increased instabilities of the flow, laminar boundary layer loses its stability and the transition to a turbulent boundary layer occurs. Ordinary RANS models cannot capture this phenomenon and they usually result in completely turbulent boundary layer. Therefore, transition models are actively being developed.

One of the transition models being actively used, that accurately predicts the transition onset characteristic of the boundary layer, is the K-kl-ω turbulence model [13][25]. It was developed by Walters and Cokljat for transition flows [25]. In this turbulence model, three equations are modeled for turbulent viscosity.

The major difference between k-kl-omega and k-omega models is the addition of third equation to the k-ω turbulence model, which represents laminar to turbulence transition phenomena.

The k-kl-omega model with the equations for turbulent kinetic energy (k_T), laminar kinetic energy (k_L) and specific dissipation rate (ω) are present in the reference of Walters and Cokljat [25].

3. Problem Setup

3.1 Geometry

The geometry of NASA Common Research Model used in the analysis was obtained from AIAA CFD Drag Prediction Workshop (originally developed by John C. Vassberg) [1] [16]. Among various configurations available wind-body configuration was chosen for the analysis (Fig. 3-1).

Geometry included original wing-body configuration, wing-body configuration with aeroelastic effects (wing bending and twist) for angles of attack from 2.5º to 4 º with 0.25 º step, which was restructured with measured deflections of test model from NASA Langley National Transonic Facility (NTF) Wind tunnel, at Re=5 million, M=0.85 [17]. Thus, both of the aerodynamic characteristics of original and deformed models can be obtained through CFD method.

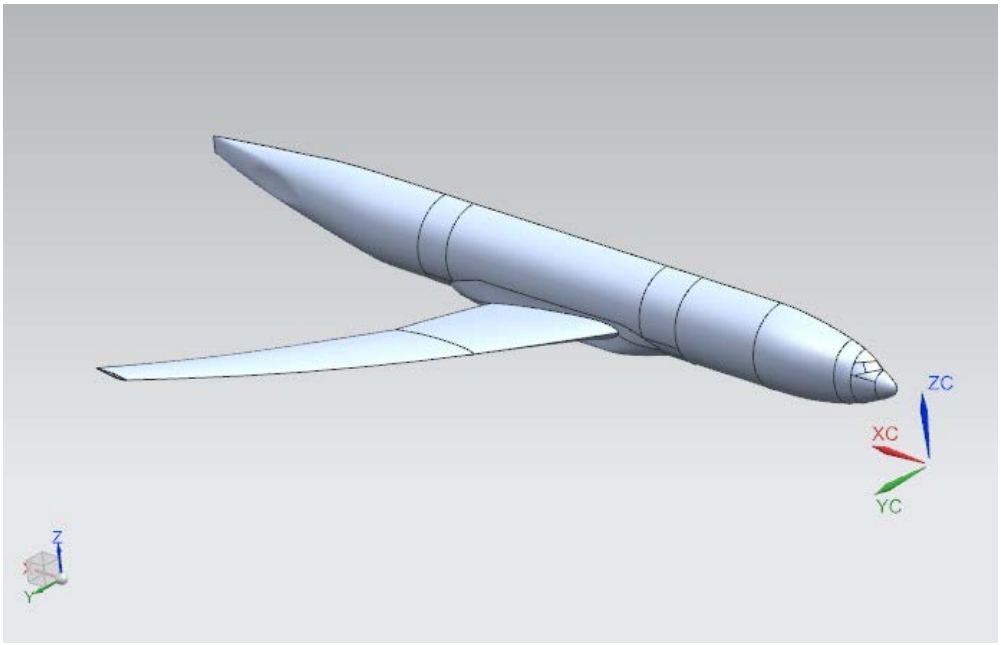

Figure 3-1. NASA CRM geometry, wing-body configuration

Original wing-body geometry is represented on Fig. 3-1. Since geometry of the aircraft model is symmetrical, symmetrical half of the aircraft model will be used for the analysis, which will help to reduce the number of elements in the computational grid, resulting in faster computational process. Comparison between the original un-deflected geometry and geometry with aero-elastic deflections from NTF Wind Tunnel on Fig. 3-2. A closer look at character of deflections for various angles of attack is represented on Fig. 3-3. There were issues importing the IGES/STEP files, mainly after import the gaps between some surface edges appeared, so geometries have been repaired first using Siemens NX CAD software [18], then some minor repairing on trailing edges and cockpit was done in Ansys Design Modeler software [19] in order to create smooth connection between aircraft geometry and flow domain.

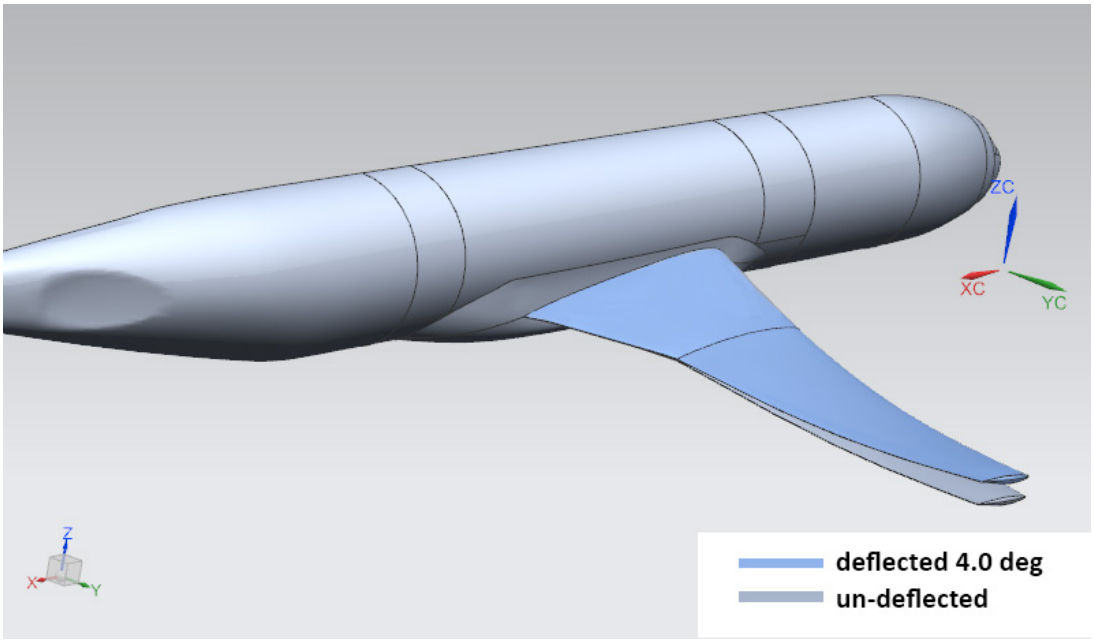

Figure 3-2. Original un-deflected geometry and geometry with deflections at AOA=4º

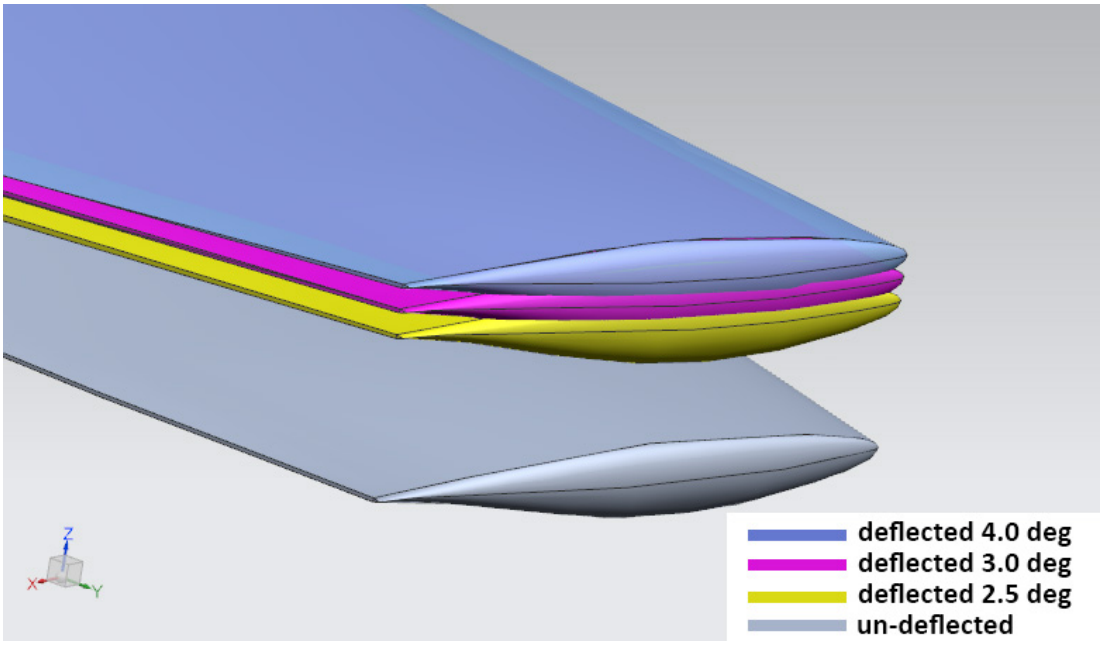

Figure 3-3. Un-deflected geometry and geometry with deflections at AOA=2.5º; 3º; 4º

The most important geometrical values for the NASA Common Research Model are presented in Table 3-1 and Figure 3-4. The coordinate system that is used id the coordinate system from original CAD file, it means X axis is longitudinal axis of the airplane, Y axis is lateral axis and Z axis is vertical axis. The dimensions of the model represent full-scale aircraft dimensions. Nevertheless, this will not influence comparison with experimental data, since the compared CFD data is compatible to compare with experimental data because the Reynolds number in both cases is the same (see Section 2.6).

Mean Aerodynamic Chord	275.8 [inch]	7 [m]
Wing Reference Area/2	297360 [inch^2]	191.84 [m^2]
Wing Span/2	1159.75 [inch]	29.458 [m]
X Moment Center	1325.9 [inch]	33.678 [m]
Z Moment Center	177.95 [inch]	4.52 [m]
Y Moment Center	468.75 [inch]	11.906 [m]
Aspect Ratio	9.0	
Angle of Sweep	35°	

Table 3-1. Reference values of NASA CRM

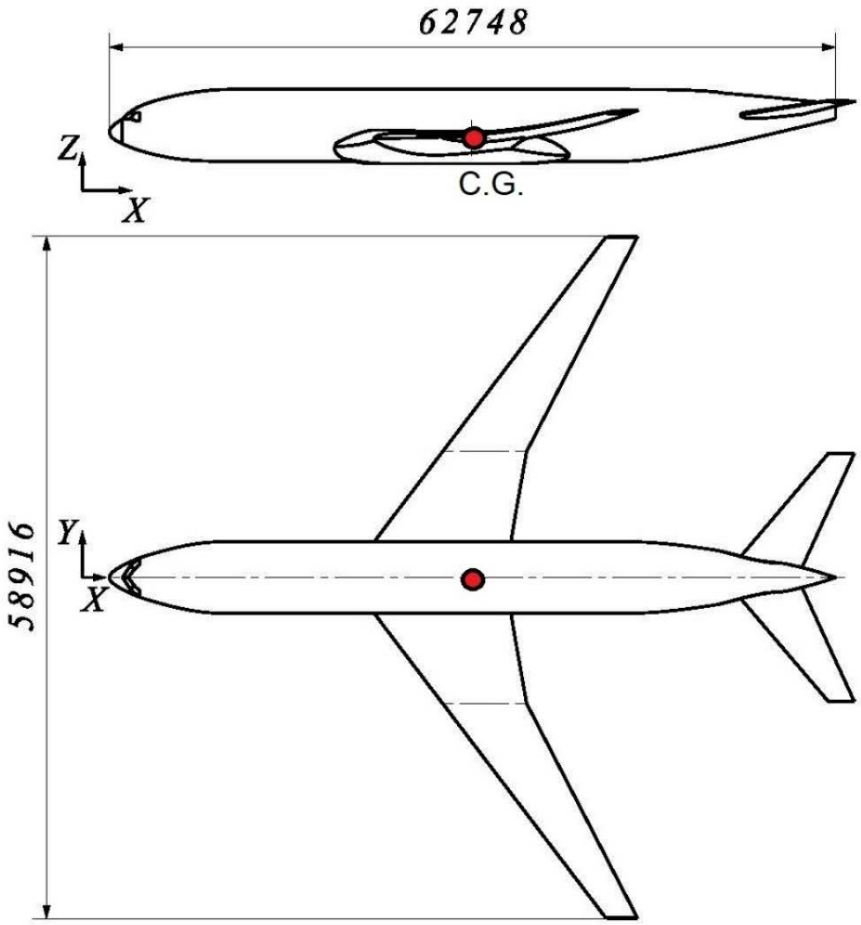

Figure 3-4. NASA CRM Full-scale dimensions in mm with position of center of gravity

3.2 Software

In this work the study of the aerodynamics characteristics is performed based on the solution of the Reynolds-averaged Navier-Stokes equations by means of the ANSYS Fluent software package [16]. Fluent uses the finite volume technique to convert the general transport equation in to a system of algebraic equations and it uses different iterative methods to solve the algebraic equations [13]. It is a key step in order to find the solution for the transport equation of a physical quantity.

ANSYS Fluent disposes two types of discrete solvers, one is pressure-based solver and another one is density-based solver, both of which make use of the finite control volume technique. The pressure-based solver originally was developed for incompressible flows, but now it is fully capable of dealing with compressible flows by use of the coupled pressure-based solver. In this work, coupled pressure-based solver is used.

The flow equations (5.2, 5.3 and 5.5) will be discretized by the second order upwind scheme. Additional equations, which are introduced by the turbulence model (Turbulent Kinetic Energy equation (5.6) and Specific Dissipation Rate equation (5.6)) will be discretized by the first order upwind scheme. The upwind discretization scheme is highly stable and can even cope with coarse level computational grids. However, the upwind scheme has disadvantage and that is that it introduces artificial dissipation to the system, which is the mathematical dissipation that stabilizes the scheme, but it is not physically present. Artificial dissipation is increased with higher gradients in the flow, thus structured computational grids are preferable with upwind schemes. Structured grids allow the user to direct and align elements according to those gradients, resulting in decrease of artificial dissipation. For this work the unstructured meshes are used (see section 5.4.1) so the arranging of the elements according to their gradients is not possible. The only way to achieve the reduction of the artificial dissipation is by refining the grid.

As for the turbulence model the two equation Shear-Stress Transport (SST) k-ω model was used in this analysis, because of its accuracy and common use in aerospace engineering (see Section 3.6 and 2.7.4).

3.3 Flow Domain

The fair field and the inlet of the flow domain and must be sufficiently far away from the airplane so that disturbances of the flow at the inlet or the far field are not noticeable at the airplane. In order to catch the wake (region of disturbed flow downstream) of the airplane, which is important in drag analysis, the outlet of the domain must also be sufficiently far away.

Considering all mentioned before, the flow domain was designed in Ansys Design Modeler [19] as a sphere with, cut in half by the symmetry plane over the longitudinal axis of the airplane (Fig 3-5). The sphere has radius of 100 MAC of the airplane, which corresponds to 700 m. A closer look on the center of flow domain with the NASA CRM model is presented on Fig. 3-6.

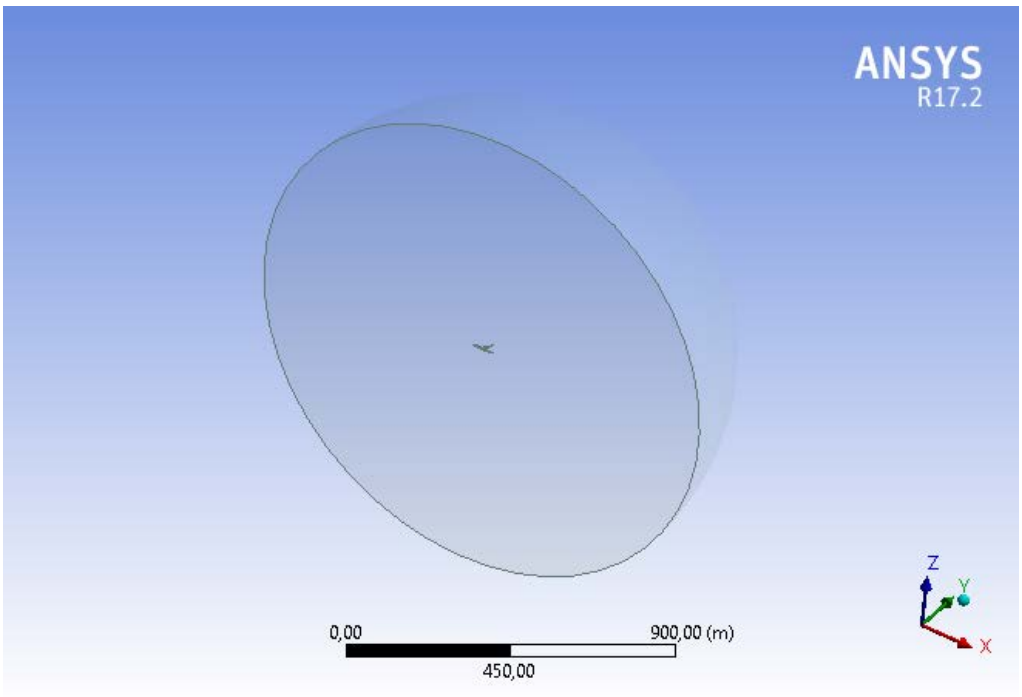

Figure 3-5. Flow Domain

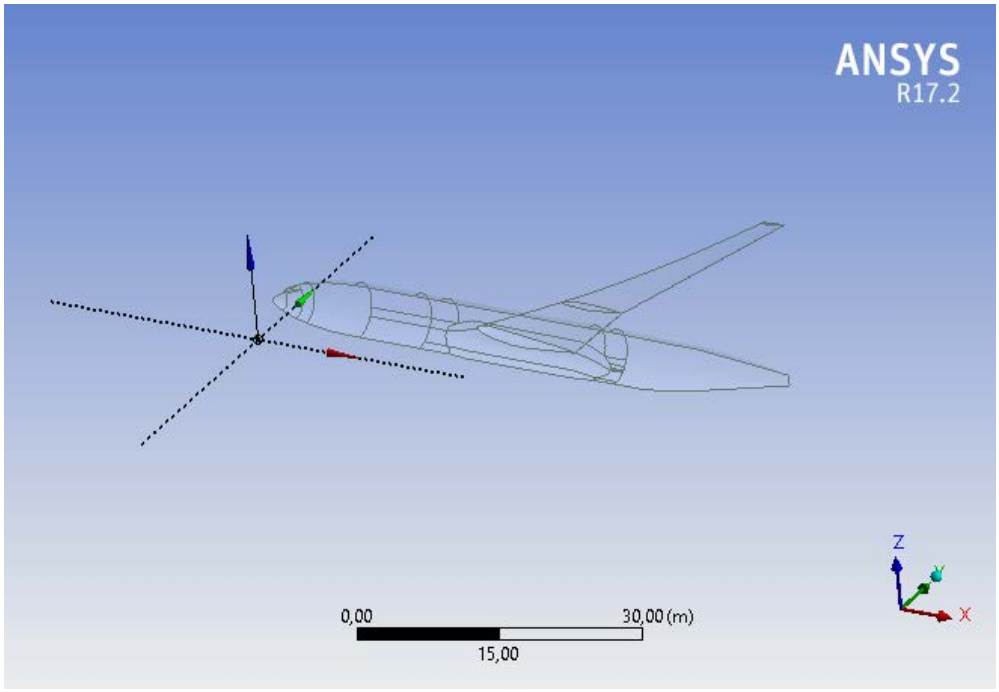

Figure 3-6. Center of the Flow Domain with NASA CRM in it

Also, the special region was designed, which encloses aircraft model plus some part of wake area behind the wing (Fig. 3-7). This region will be used as during grid creation process as a region called body of influence, where the grid density will be higher compared to the rest of the domain. The volume of the body of influence is approximately twice of volume of aircraft model.

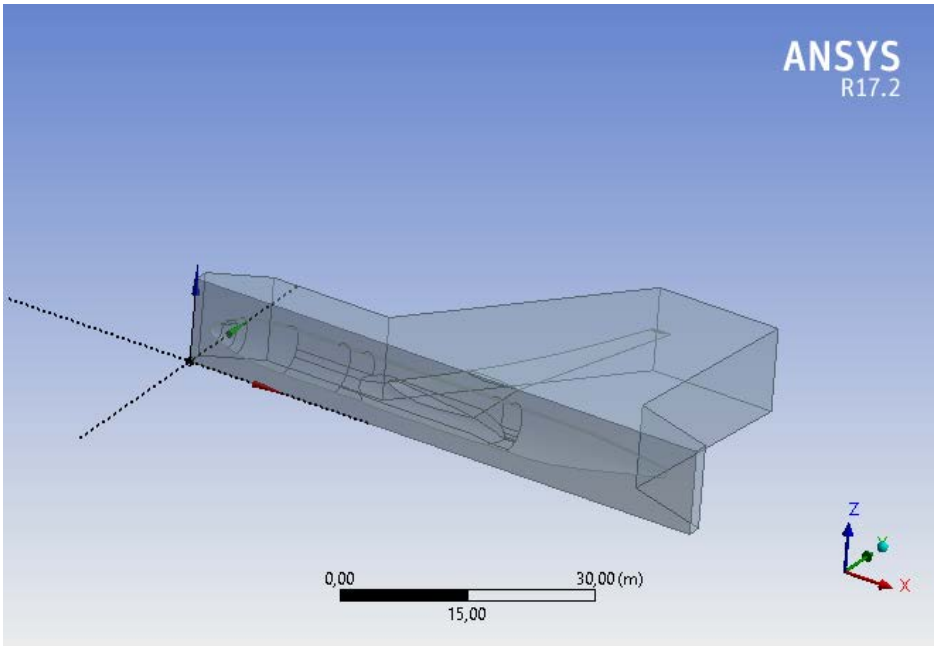

Figure 3-7. Higher grid density region (body of influence)

3.4 Boundary conditions

In order to define a problem that results in a unique solution, it is necessary to specify information on the dependent variables at the flow domain boundaries. The flow domain contains 3 sets of surfaces which are used for setting up the boundary conditions.

Symmetry plane

The plane which passes thought the longitudinal axis of the aircraft (plane of symmetry of the sphere) is set the boundary condition “symmetry plane”.

Far field

The outer surface of the half-sphere is set the boundary condition “pressure far field” with Mach number equal to 0.85 with the direction which represents the corresponding angle of attack.

Aircraft surface

The aircraft model surface is being set the boundary condition “wall”. This will ensure the velocity to zero at the aircraft surface. This technique is no-slip boundary condition [13].

The roughness height and roughness constant are not known, therefore this is set to default, which is 0 and 0.5 respectively.

3.5 Grid Design

Computational Grid (or Mesh) is defined as a small geometry shapes (cells), which are formed after discretization of geometric domain. Briefly, the grids can be classified into two types: structured grids and unstructured grids. The simplest one is structured grid, where all nodes have the same number of elements around the grid [13]. It is easily described and stored. But this grid is generally more suitable for the simple domain.

As for the unstructured grid, in general, this type of grid is well suitable both for the complex and simple geometries. This type of grid is very popular in CFD. The disadvantage of it lies in the irregularity of data structure, because of that the grid is more difficult to describe and store.

Generating a good quality grid is a key step to obtain a correct solution. In order to perform quality discretization of the complex geometry, such as the aircraft model, the grid should have enough elements and also include a boundary layer to solve the turbulence equations. For the final analysis several models have to be build. Also, since the flow near the aircraft model is very important and complex, a very fine grid is needed at the center of the domain where the aircraft geometry is present. Far away from the aircraft geometry, the flow is comparably simple, thus the coarse grid can be used. Because of this the special geometry region was created, which encloses aircraft model plus some part of wake area behind the wing (body of influence, see section 3.1).

3.5.1 Choice of elements

There is a wide range of elements, which are available for mesh creation. The basic 3-D elements are tetrahedron, quadrilateral pyramid, triangular prism, and hexahedron. For this work the unstructured tetrahedron (tetra) grid was used (Fig. 3-8). The tetra element was used because it is very universal, it can be used for difficult geometries without much user input. The grid was created in in ANSYS Meshing software [21]. The boundary layer was created with help of the inflation tool (see section 3.5.2).

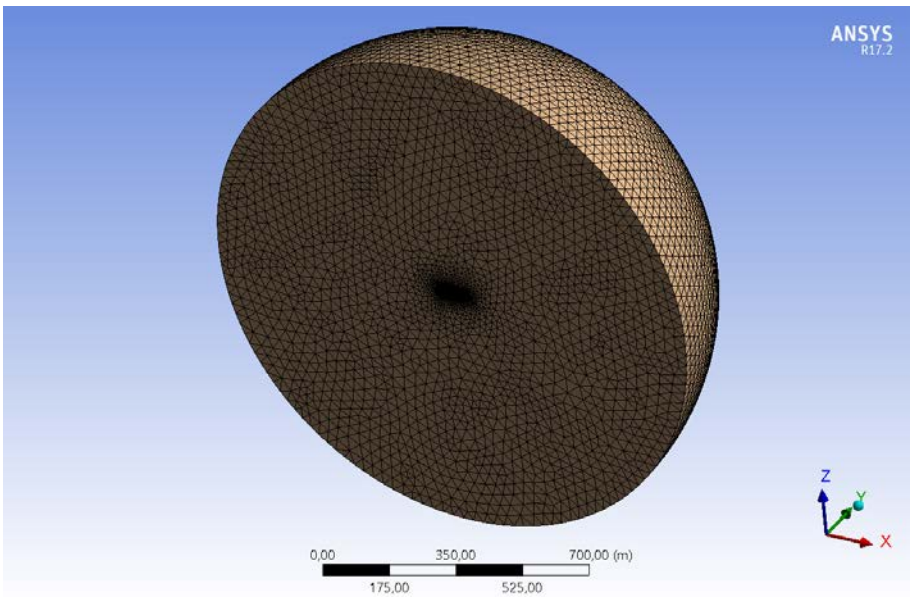

Figure 3-8. Computational Grid

3.5.2 Boundary layer

The boundary layer is created using inflation in ANSYS Meshing. Inflation creates a boundary layer around the whole aircraft model consisting of quad elements (Figure 3-9), which is useful for the solution of the turbulence model. In order to define how fine and thick the boundary layer must be, the computation with help of the y+ value is required [24]. The y+ value is a non-dimensional parameter that represents how fine is the boundary layer. It is defined by equation (2-13).

$$y^+ = \frac{\rho\, u_f\, \Delta y_1}{\mu} \qquad \text{(eq. 2-13)}$$

Where u_f represents friction velocity, Δy_1 is the first cell height. The chosen k-ω SST turbulence model (see section 3.7) has a requirement $y^+ < 300$. In order to capture even the low Reynolds number behavior an $y^+ < 1$ is recommended, so a low y+ value is desirable. The friction velocity is approximated with equation (2-14), which is an empirical based estimation [23].

$$u_f = 0{,}058 \cdot Re^{-0{,}2} \qquad \text{(eq. 2-13)}$$

By combining equation (2-13) and (2-14) the equation for the first layer height is obtained:

$$\Delta y_1 = \frac{y^+ \mu}{\rho\, u_f} \qquad \text{(eq. 2-15)}$$

For the grid used in the analysis the number of layers in the boundary layer is set to 30, the first layer height is set to 1e-4 m and the growth rate is set to 1.4. For the grids which were developed during grid independence study the values differ, except the growth rate which is set to 1.4 (see section 3.5.3).

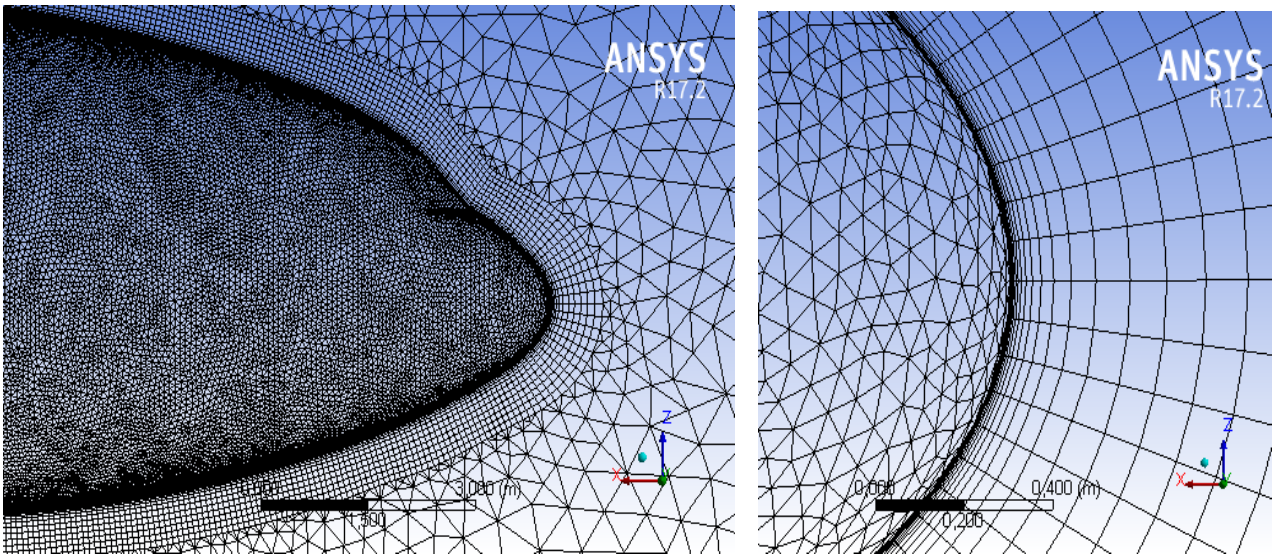

Figure 3-9. Boundary layer mesh at the aircraft model with detailed view at the nose

3.5.3 Grid independence study

Several grids were built in order to understand the grid influence on the results of CFD calculation. The geometry that was chosen for grid independence study was wing-body configuration with aeroelastic effect deflection at angle of attack 3.75º.

After several design iterations, four grids were examined in final. The grid are unstructured tetra grids with inflation layer, which differ in the number of elements (Table 3-2) (Fig. 3-10, 3-11, 3-12, 3-13).

GRID	nodes	elements
Level 1	175708	665216
Level 2	318721	1161963
Level 3	991716	3060448
Level 4	2730809	6846697

Table 3-2. Grids with different element size

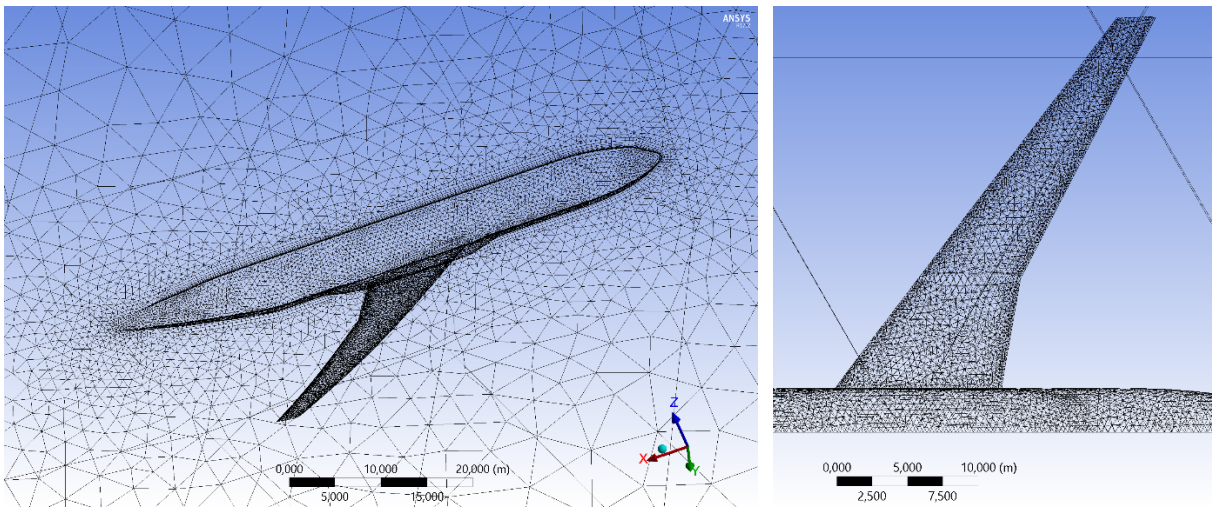

Figure 3-10. Grid Level 1

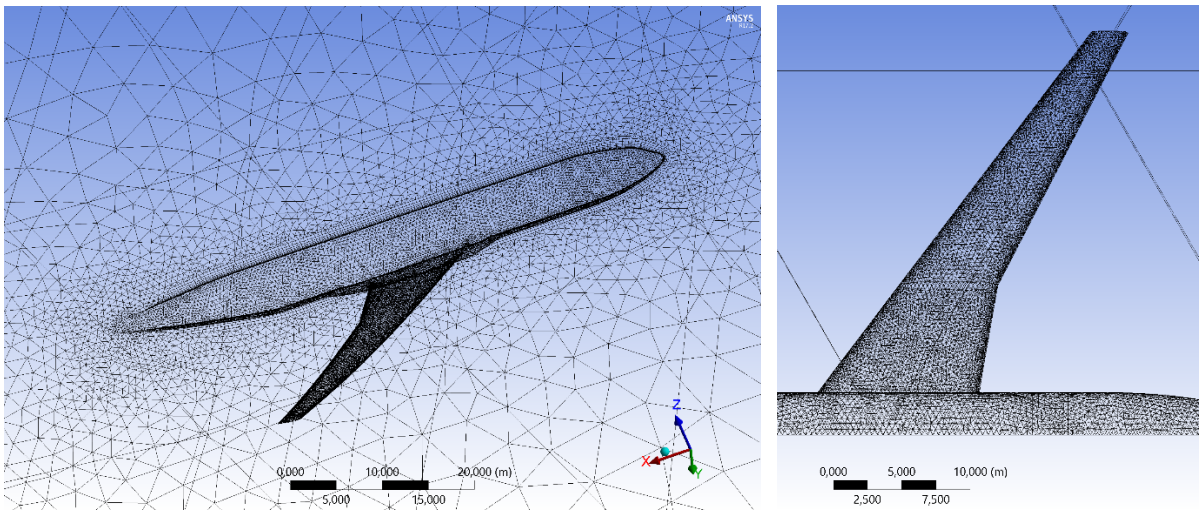

Figure 3-11. Grid Level 2

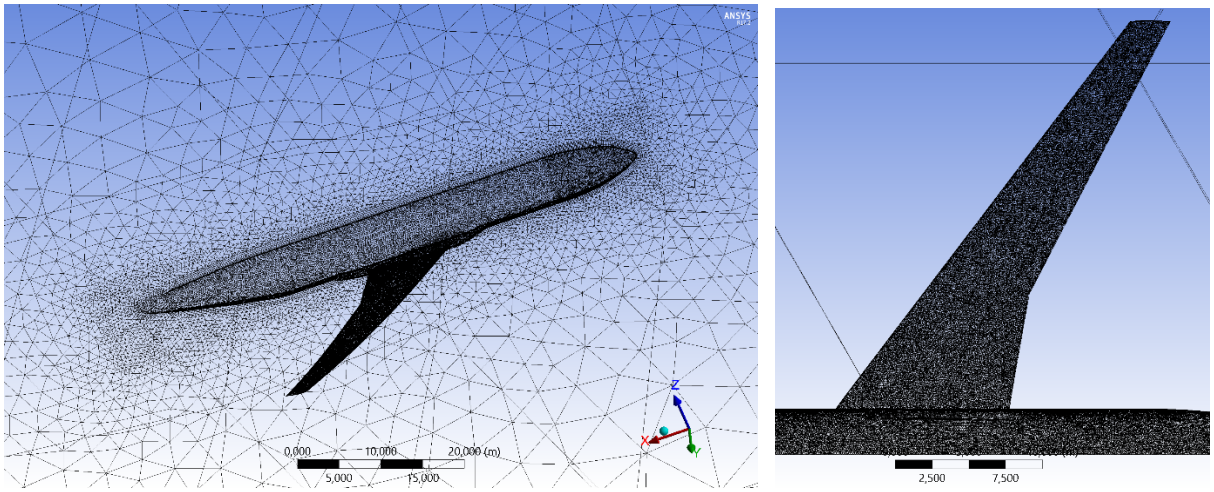

Figure 3-12. Gird Level 3

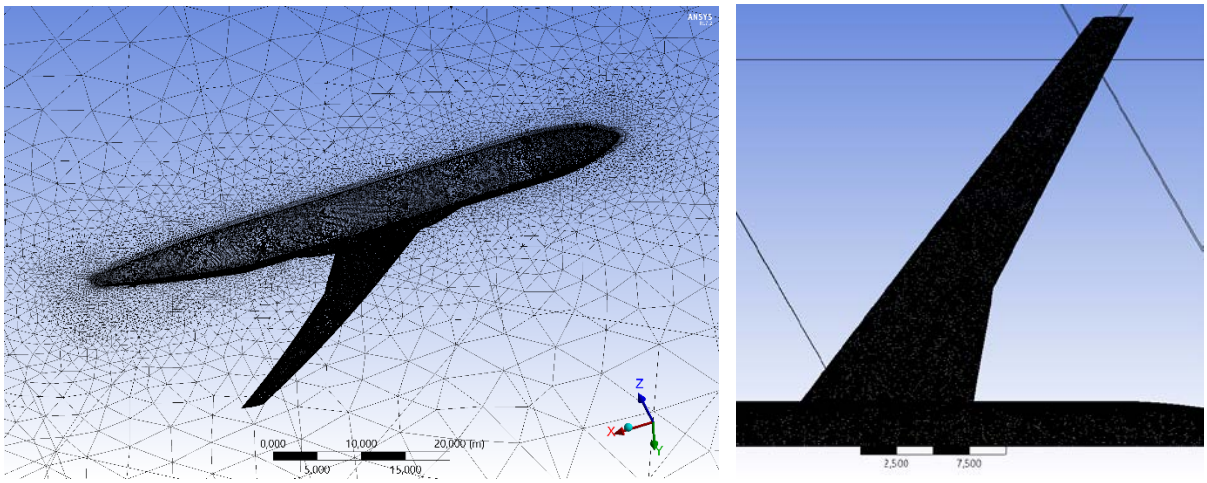

Figure 3-13. Grid Level 4

The size function in ANSYS Meshing is set to Proximity and Curvature. The global grow rate for the mesh is set on 1.2 and it is the same for all grids. The meshing algorithm was chosen to be patch confirming method, which means that the meshing process starts first from edge, face and then body. In this case all faces and their boundaries are respected and meshed, which is suitable for complex geometries like aircraft.

Some parts are meshed with a local mesh size. For example, the wing is meshed with a local mesh size, because the flow around this part is important since it contains high pressure and velocity gradients. The difference in local mesh sizing of the corresponding grids can be found in table below.

	Element size [m]			
Part	**Level 1**	**Level 2**	**Level 3**	**Level 4**
body of influence region	1	0,75	0,5	0,5
leading edge of the wing	0,2	0,1	0,1	0,075
trailing edge of the wing	0,2	0,1	0,1	0,075
wing	0,5	0,3	0,15	0,1
wingtip	0,3	0,2	0,1	0,075
fuselage	0,5	0,4	0,2	0,1
cockpit	0,5	0,3	0,15	0,075
nose	0,5	0,3	0,15	0,075
number of inflation layers	20	20	30	30
the first layer height	0,001	0,001	0,0001	0,0001

Table 3-3. Local mesh size for different grids

Using the same test conditions as in the wind tunnel (see Section 4.1) the computation was performed in ANSYS Fluent software and necessary aerodynamic characteristics were obtained for comparison study. The solutions converged after around 200 iterations, after which the values of drag coefficient Cd, lift coefficient Cl, moment coefficient Cm were obtained. The procedure of convergence is shown on next figures.

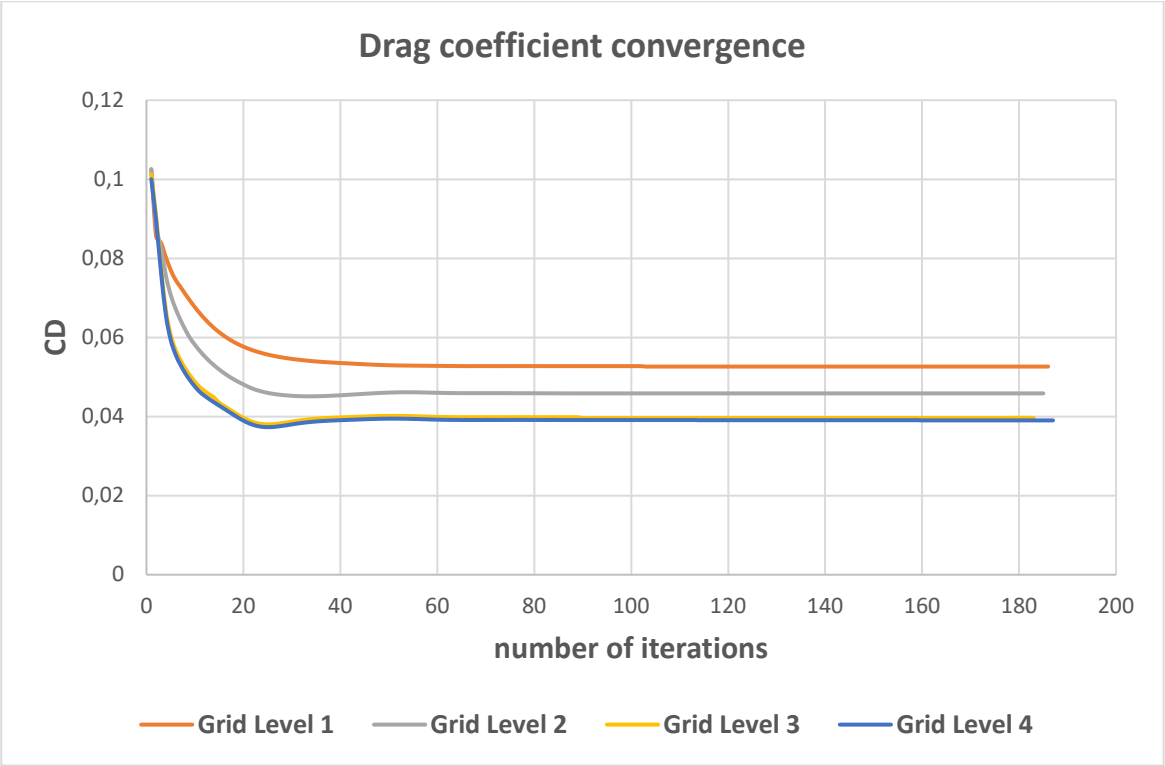

Figure 3-14. Convergence of the drag coefficient

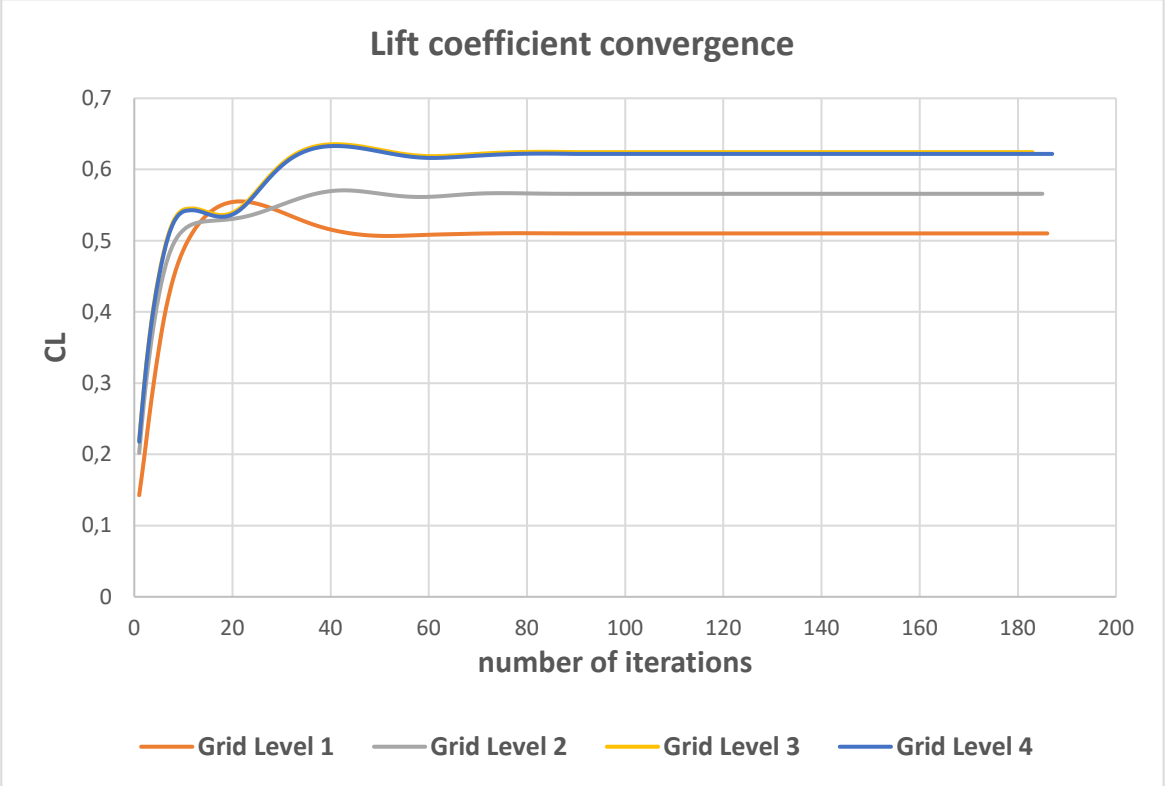

Figure 3-15. Convergence of the lift coefficient

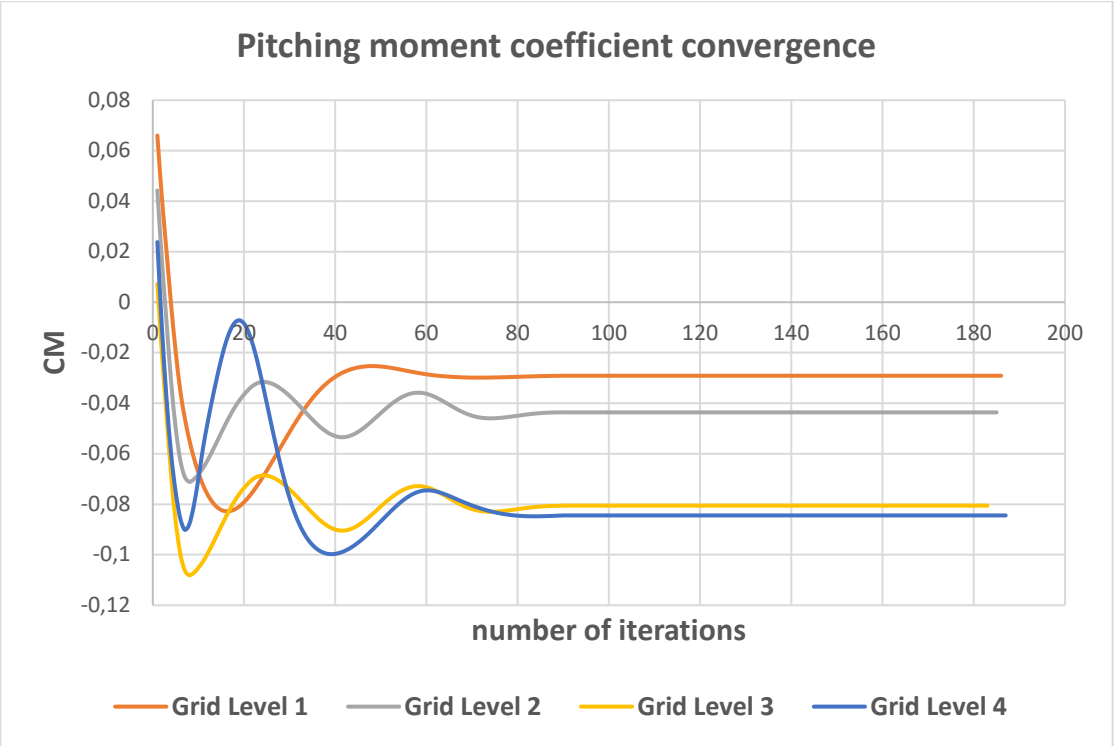

Figure 3-16. Convergence of the moment coefficient

The results of the calculation are presented in Table 3-4. It is possible to see that obtained aerodynamic characteristics are changing depending on the grid size.

GRID	Level 1	Level 2	Level 3	Level 4
CD	0,0526	0,0459	0,0397	0,0390
CL	0,5103	0,5659	0,6244	0,6219
CM	-0,0291	-0,0436	-0,0806	-0,0844

Table 3-4. Obtained aerodynamic characteristics depending the grid size

Percentage of change between:	Level 2 & 1	Level 3 & 2	Level 4 & 3
CD	12,88%	13,51%	1,60%
CL	10,88%	10,35%	0,41%
CM	49,79%	84,85%	4,75%

Table 3-5. The change of the obtained values after each grid refinement

Each obtained value of the finer grid was compared to corresponding value of the coarse grid, i.e Grid Level 2 was compared with Grid Level 1 and so on, in order to see how the values are changing with every grid refinement (Table 3-5). According to obtained data the percentage of change of values between Grid Level 3 and 4 is less than 5%, therefore it is possible to conclude that further grid refinement will not have significant impact on the calculated results. Consequently, Grid Level 3 is chosen as optimal for further calculations.

3.6 Turbulence model selection

The given problem requires the use of turbulence models, since the turbulence in the flow occurs due to high Reynolds numbers (see section 2.7). In this section the couple of turbulence models, which are discussed before, are examined, such as Realizable k-epsilon model, standard k-omega model, SST k-omega model and K-kl-omega transition model (see section 2.7).

The computational grid that was chosen for turbulence models comparison study was the same grid that was used during grid independence study (see section 3.5.3) i.e. Grid Level 3 of wing-body configuration with aeroelastic effect deflection at angle of attack 3.75º. Using the same test conditions as in the wind tunnel (see Section 4.1) the computation was performed in ANSYS Fluent software and aerodynamic characteristics were obtained and compared.

In the Fluent the process of convergence can be monitored not only examining the fluctuations as the desired values but also looking at so called residuals values during the computation process. In this work default settings of convergence criteria were used in Fluent i.e. solution is considered converged when residuals decrease to the value of 1e-03, except the residual of energy which should decrease to the value of 1e-06. The residuals during computation process in Fluent using different turbulence models are shown on Figures 3-17, 3-18, 3-19, 3-20.

From the figures it is possible to see that for Realizable k-epsilon and K-kl-omega there was oscillation of residual values, especially for omega and epsilon, while the values for k-omega standard and SST remained in relatively smooth path. This indicated that k-omega standard and SST can be more suitable for the solution given problem as they experience higher stability.

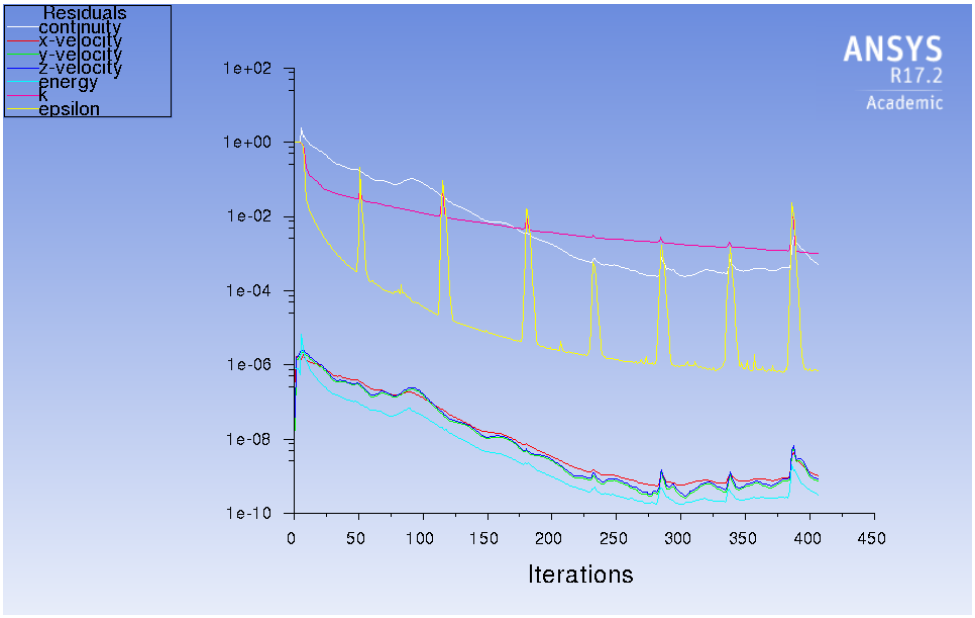

Figure 3-17. Residuals during the calculation with use of Realizable k-epsilon model

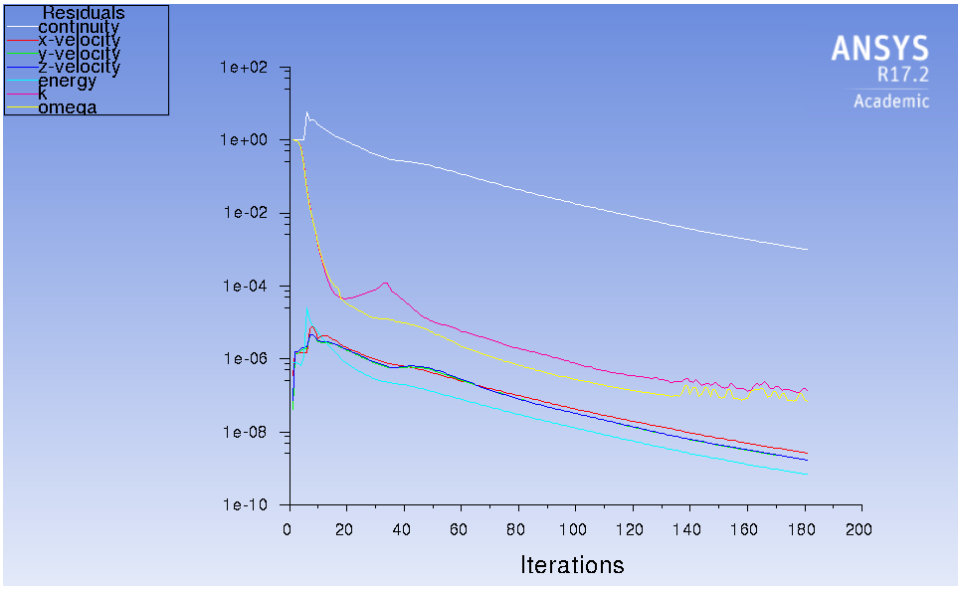

Figure 3-18. Residuals during the calculation with use of standard k-omega model

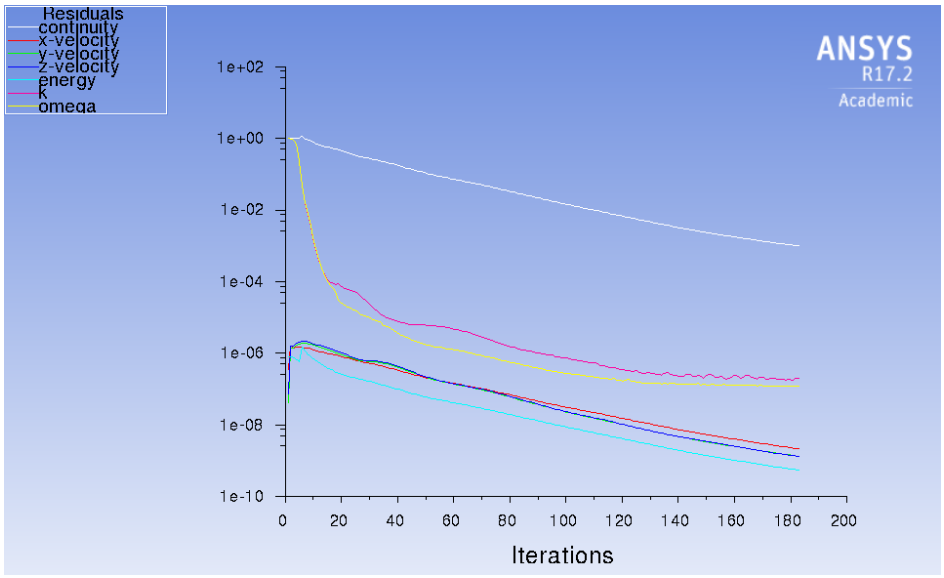

Figure 3-19. Residuals during the calculation with use of SST k-omega model

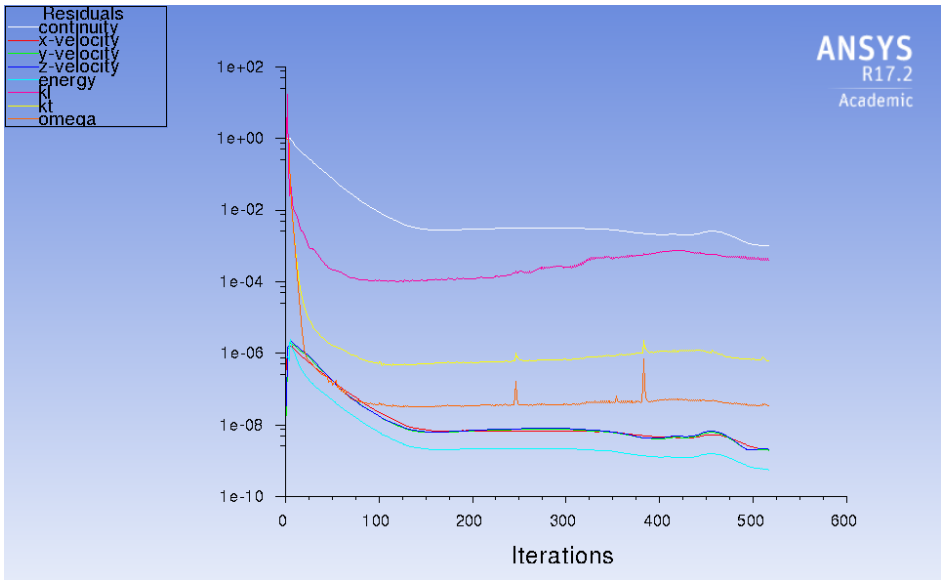

Figure 3-20. Residuals during the calculation with use of K-Kl-omega transition model

The convergence of the solutions was different for each turbulence model. The solution with realizable k-epsilon model converged after approximately 400 iterations. The solution with standard k-omega and SST k-omega were converged almost simultaneously, after around 200 iterations. The solution with K-kl-omega transition model was the last, converging after around 500 iterations. The procedure of convergence for drag coefficient, lift coefficient and pitching moment coefficient is shown on next figures.

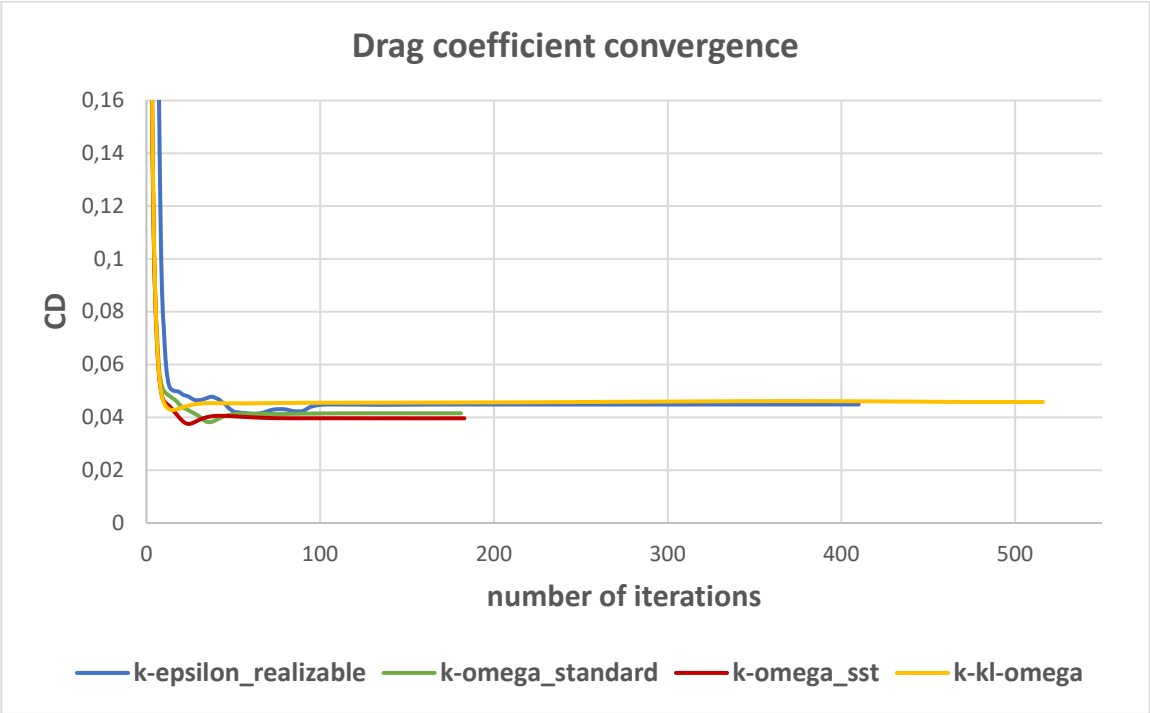

Figure 3-21. Process of convergence of drag coefficient for different turbulence models

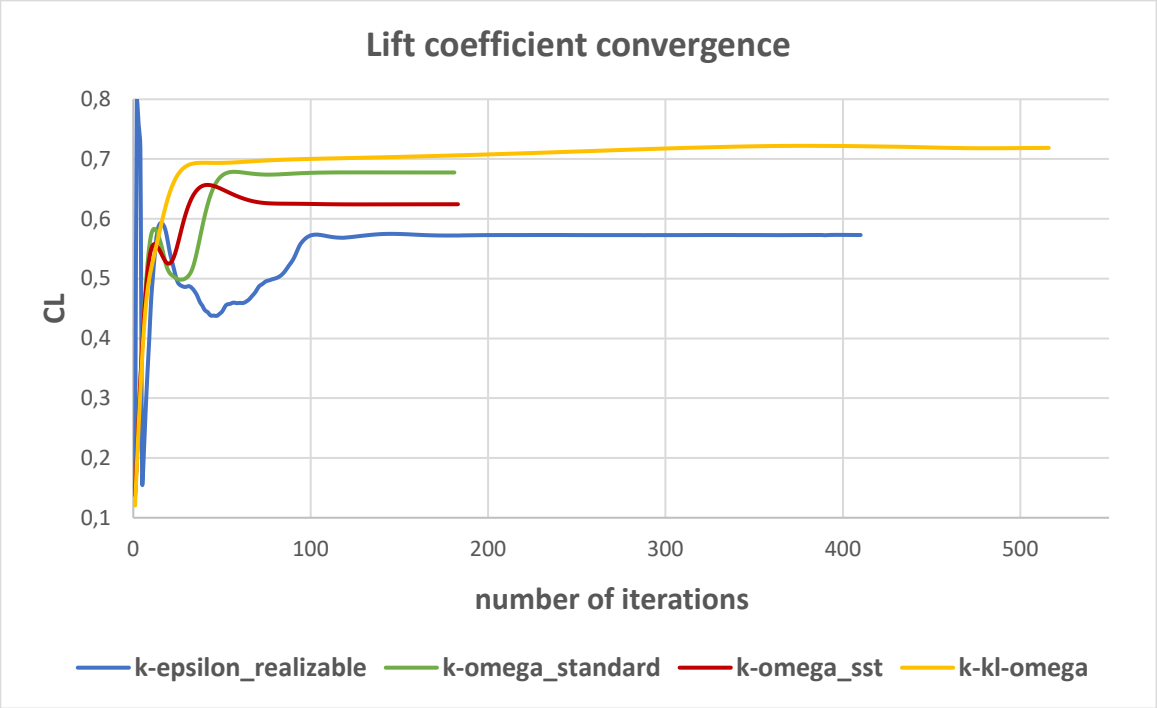

Figure 3-22. Process of convergence of lift coefficient for different turbulence models

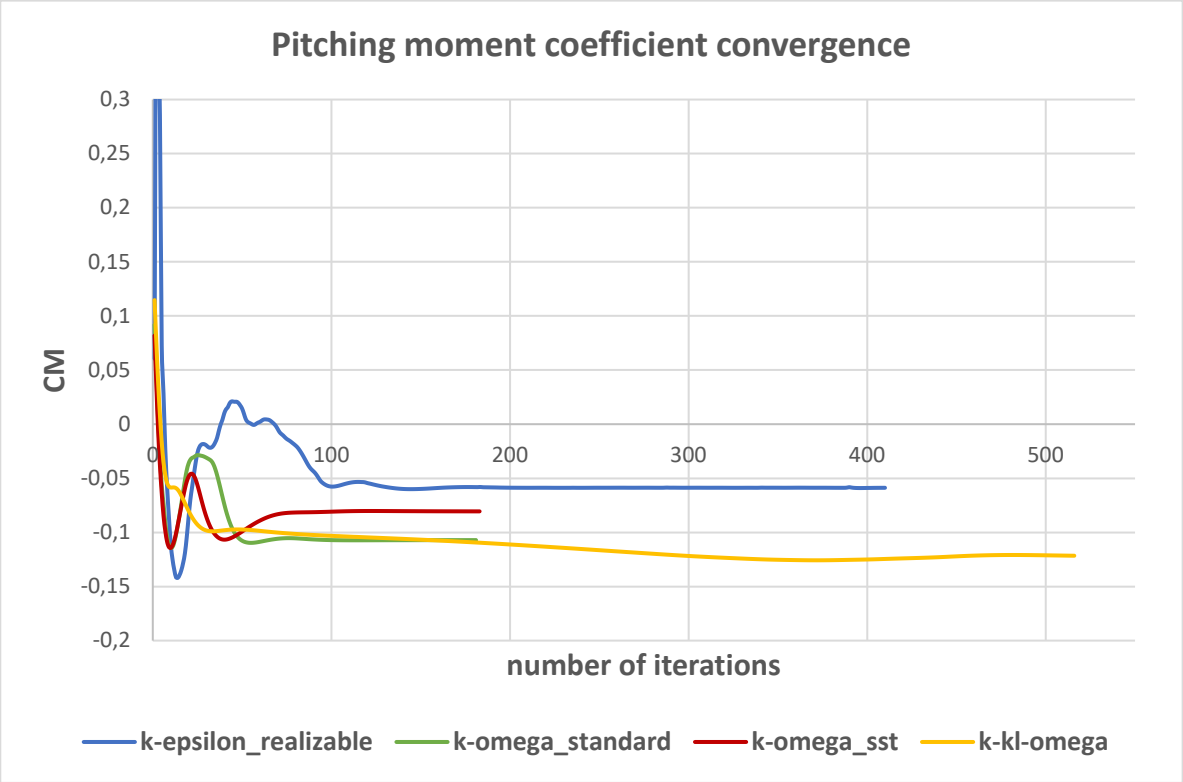

Figure 3-23. Pitching moment coefficient convergence for different turbulence models

The results of the calculations are presented in Table 3-5. It is possible to see that obtained aerodynamic characteristics differ with each turbulence model.

	Realizable k-ε	Standard k-ω	SST k-ω	K-kl-ω
CD	0,0449	0,0415	0,0397	0,0458
CL	0,5730	0,6775	0,6244	0,7187
CM	-0,0588	-0,1071	-0,0806	-0,1216

Table 3-6. Obtained aerodynamic characteristics with use of different turbulence models

The obtained results were compared to experimental results from NTF Test 197 Run 44 [17] (see Section 4.3 Table 4-4). In this way, the Realizable k-ε model underpredicts the lift by around 7% and overpredicts the drag by 21%. Standard k-ω model overpredicts both lift and drag by around 10% and 12% respectively. The SST k-ω model performs a good prediction of the lift and drag, that differs from experimental data only on 1,5% and 7% respectively. The K-kl-ω transition model overpredicts drag by 23% and lift prediction differs on 17% compared to experimental results. All turbulence models have overpredicted the behavior of the pithing moment, this is possible due to the absence of supportive mechanism (sting) in CFD model. The results of comparison can be seen in Table 3-7.

CFD vs NTF data	Realizable k-ε	Standard k-ω	SST k-ω	K-kl-ω
CD	20,87%	11,86%	6,78%	23,43%
CL	6,93%	10,05%	1,43%	16,74%
CM	11,47%	61,34%	21,35%	83,09%

Table 3-7. Percentage change compare to experimental results from NTF

According to obtained data, SST k-ω model is chosen for father calculations, as it has good accordance with experimental results from the wind tunnel and it offers stability and fast convergence of the computed results.

4. Computation & Results

4.1 Flow conditions

The flow conditions were setup to match Langley National Transonic Facility test conditions: Test 197, Run 44 for Re=5 mln, M=0.85 [17]. The values are presented in the table below.

Reynolds number based on mean aerodynamic chord [1]	$5*10^6$
Mach number [1]	0.85
Total Pressure [Pa]	210221.15
Total Temperature [K]	322.72

Table 4-1. Flow condition of NTF Wind Tunnel Test 197, Run 44

4.2 Fluent setup

As mentioned before, computation is performed in the ANSYS Fluent software package [16] which enables to solve Reynolds-averaged Navier-Stokes equations by means of the finite volume technique which converts the general transport equation in to a system of algebraic equations. The solver chosen for the calculation is pressure-based couple solver (see Section 3.2) and the turbulence model is chosen to be k-ω SST model (see Section 3.6).

The boundary conditions on the boundaries of the flow domain are set to "symmetry plane" and "pressure far field", the aircraft surface is set to the boundary condition "wall" (see section 3.4). In the pressure far field boundary condition the velocity is specified by the Mach number M=0.85 and the direction ($cos(AOA)$, 0, $sin(AOA)$) which means the flow has direction vector with two components: $cos(AOA)$ in X-direction and $sin(AOA)$ in Z-direction. The table below illustrates corresponding flow direction components.

AOA [°]	**2,5**	**2,75**	**3**	**3,25**	**3,5**	**3,75**	**4**
X-component	0,999048	0,998848	0,998630	0,998392	0,998135	0,997859	0,997564
Z-component	0,043619	0,047978	0,052336	0,056693	0,061049	0,065403	0,069756

Table 4-2. Flow direction components

The results obtained from CFD will be compared with experimental data obtained during the test 197 in NTF Wind Tunnel [17]. To match the experimental data, the Reynolds number must correspond to the Reynolds number used during the test in NTF. In this work, equality of the Reynolds numbers is achieved by scaling aircraft model geometry, as shown in Table 4-3. For matching Re=5 mln the scale factor is 0,0184.

	MAC [m]	Area/2 [m^2]	wingspan/2 [m]	Moment center X [m]	Moment center Z [m]	Moment center Y [m]
original	7	191,84	29,458	33,678	4,52	11,906
scaled	0,1288	0,065287	0,54203	0,619675	0,083168	0,21907

Table 4-3. Comparison of the original and scaled geometry

The Grid Level 3 with 339447 nodes and 1450206 elements was chosen for the following analysis. It consists from tetra elements and has boundary layer with quad elements covering aircraft model geometry (see Section 3.5.3). The Fluent interface with scaled grid is shown on the figure below.

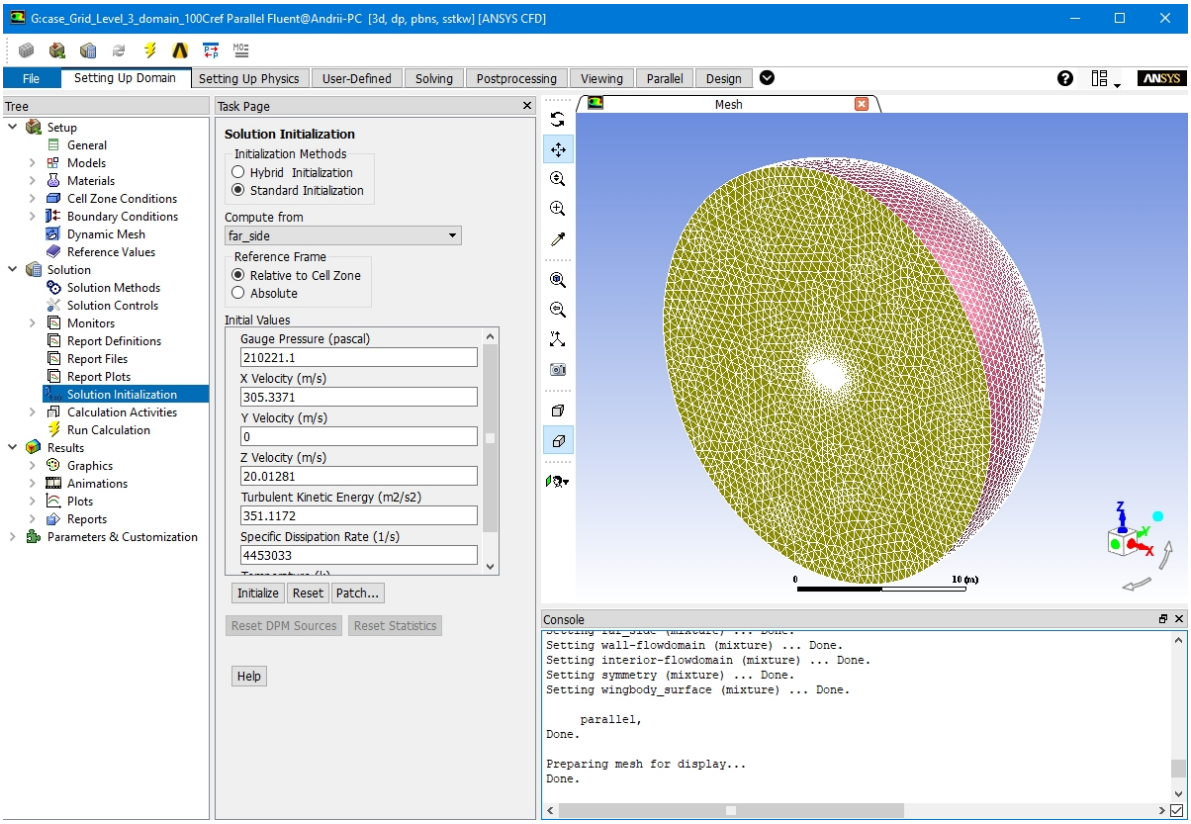

Figure 4-1. Fluent with scaled mesh

The summary of the Fluent setup can be represented as following:

General:

- Solver type: Pressure-Based

Models:

- Energy: On
- Viscous: k-omega (2 eqn), k-omega model: SST, compressibility effects

Materials:

- Fluid: Air, density – Ideal Gas Law, viscosity - Sutherland Law

Boundary conditions: (see Section 3.4 and Table 4.2)

Reference values:

- Area: 0.065287 m^2
- Length: 0.1288 m

Solution methods:

- Scheme: Coupled, Pseudo Transient, High Order Term Relaxation

Solution Initialization:

- Standard Initialization

4.3 Aerodynamic coefficients

The computation was performed for angle of attack 2.5-4º with 0.25º step for original un-deflected geometry and geometry with aeroelastic effect deflections accordingly. Flow conditions were specified according to NTF test conditions. Each case was running 200 iterations, which was enough for results to converge. The obtained data was compared to NTF Test 197 Run 44 data (Table 4-4).

ALPHA	2,47	2,66	2,89	3,17	3,40	3,67	3,90	4,15
CD	0,0225	0,0238	0,0259	0,0289	0,0318	0,0353	0,0390	0,0433
CL	0,4568	0,4861	0,5205	0,5585	0,5848	0,6087	0,6226	0,6391
CM	-0,0592	-0,0623	-0,0677	-0,0728	-0,0732	-0,0693	-0,0635	-0,0558

Table 4-4. NTF Wind Tunnel data, Test 197 Run 44, Re=5 mln, M=0.85

The obtained aerodynamic characteristics for the original un-deflected geometry and geometry with aeroelastic effect deflections are represented in the Table 4-5 and 4-6 as well as on Figures 4-2, 4-3, 4-4.

ALPHA	2,5	2,75	3	3,25	3,5	3,75	4
CD	0,0295	0,0320	0,0350	0,0383	0,0419	0,0456	0,0497
CL	0,5519	0,5856	0,6177	0,6454	0,6671	0,6826	0,6952
CM	-0,0936	-0,0979	-0,1020	-0,1033	-0,1003	-0,0925	-0,0815

Table 4-5. CFD data: aerodynamic coefficients for undeformed case

ALPHA	2,5	2,75	3	3,25	3,5	3,75	4
CD	0,0252	0,0281	0,0305	0,0330	0,0355	0,0397	0,0443
CL	0,4823	0,5091	0,5443	0,5775	0,6003	0,6244	0,6528
CM	-0,0739	-0,0759	-0,0834	-0,0874	-0,0883	-0,0806	-0,0752

Table 4 6. CFD data: aerodynamic coefficients for case with aeroelastic effect deformation

ALPHA	2,5	2,75	3	3,25	3,5	3,75	4
CD	14,5%	12,3%	12,6%	13,8%	15,3%	13,1%	10,8%
CL	12,6%	13,1%	11,9%	10,5%	10,0%	8,5%	6,1%
CM	21,0%	22,4%	18,2%	15,3%	11,9%	12,9%	7,7%

Table 4-6. Change in CFD data of the deformed case compare to the undeformed case expressed in percentages

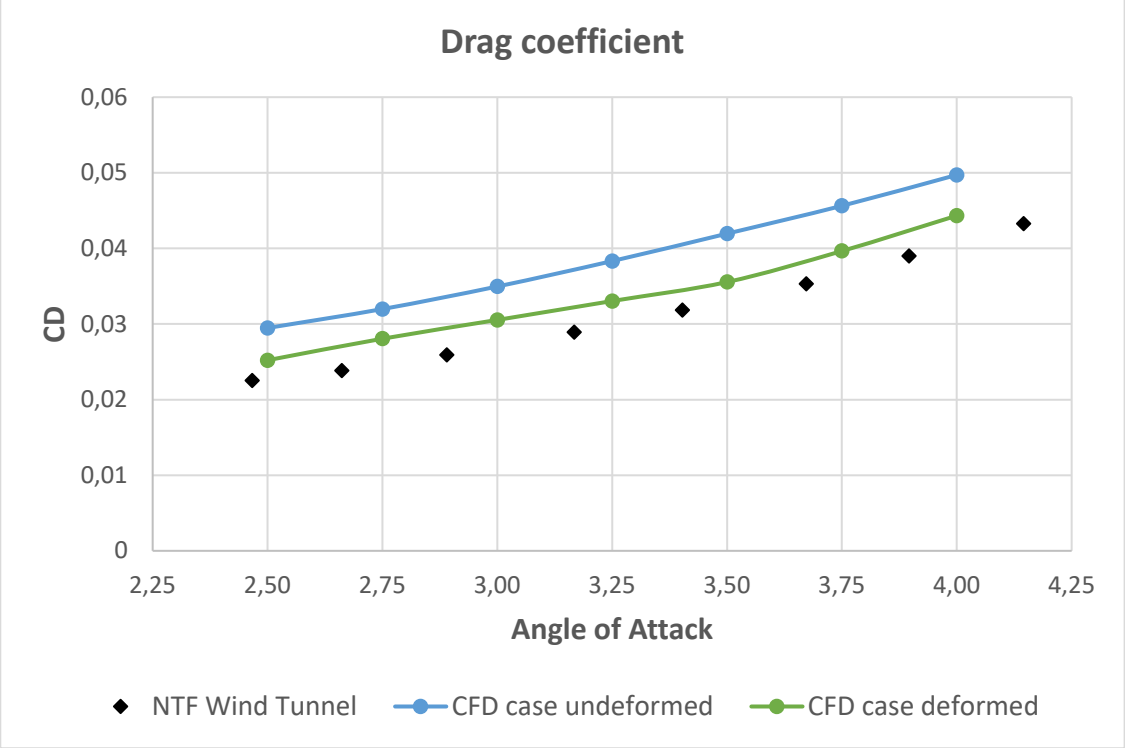

Figure 4-2. Drag coefficient for original geometry, deformed geometry and experimental data from NTF

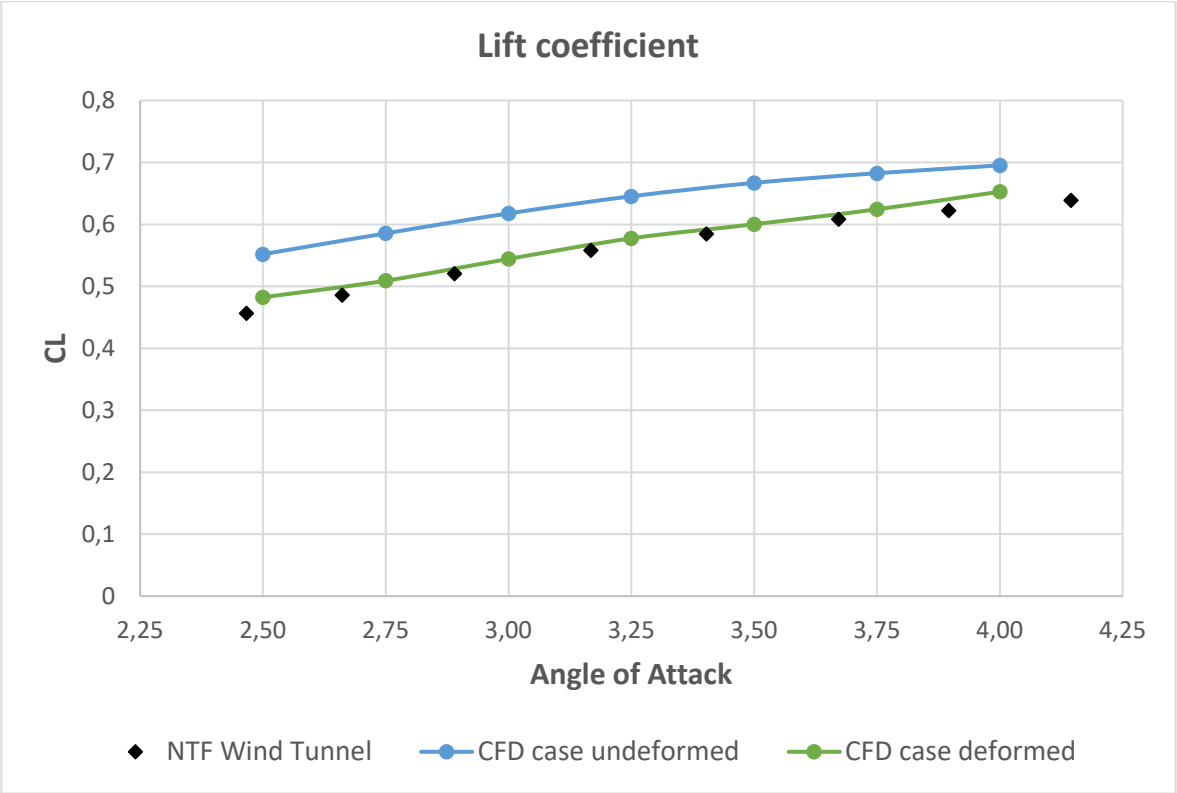

Figure 4-3. Lift coefficient for original geometry, deformed geometry and experimental data from NTF

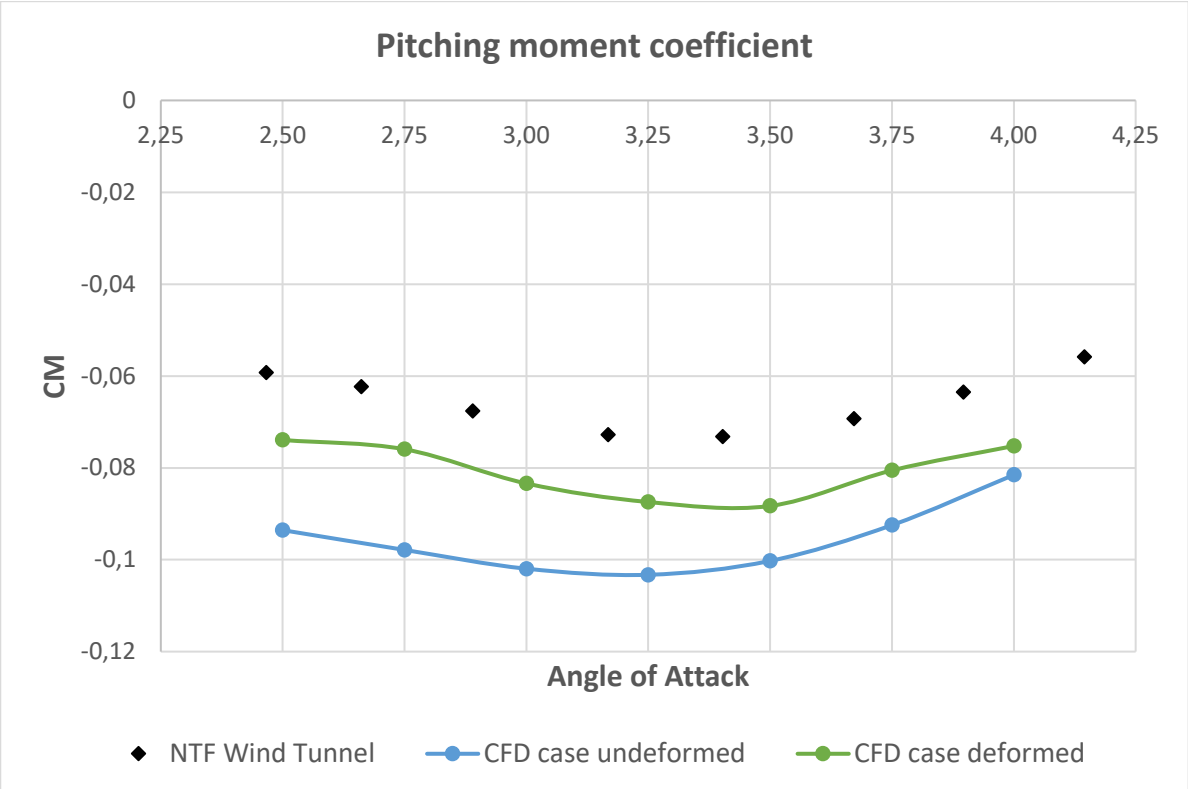

Figure 4-4. Pitching moment coefficient for original geometry, deformed geometry and experimental data from NTF

Graphical representations of the obtained aerodynamic coefficients for the rigid and deformed geometry are presented on Figures 4-2, 4-3 and 4-4. It is possible to see that deformed aircraft model gives a better match between the CFD and experimental data.

A good agreement with experimental data is obtained for the lift coefficient of the deformed geometry. The drag coefficient agreement is slightly worse while the pitching coefficient agreement is not very good. The computed pitching moment coefficients are larger compared to the ones obtained from the experiment. This happens due to the presence of aircraft model supportive mechanism (sting) in wind tunnel, which influences pitching moment behavior.

The reason of larger values of computed drag coefficient can lie in the coarser mesh near wing leading edge and the nose of the fuselage. Also, the presence of sting in wind tunnel can have an influence on drag as well.

From the obtained data it is possible to see that effect of deformation decreases the lift coefficient by 10% on average, the drag coefficient is as well decreased by 13% on average. The pitching moment coefficient experiences a decrease by 16% due to the effect of deformation.

4.4 Pressure coefficient distributions

The pressure coefficient distribution was measured in four sections of the wing: Section 1 corresponds to 13,1% of half-wingspan, Section 5 corresponds to 50,2% of half-wingspan, Section 7 lies in 72,7% of half-wingspan, Section 9 lies in 95% of half-wingspan (Fig. 4-5). The results were compared to NTF Wind Tunnel data from corresponding wing section.

In this chapter pressure distribution for section 7 and 9 will be presented, since those are the sections of the wing that experience the biggest wing deformation, therefore they are the most interesting regarding the change of aerodynamic characteristics due to deformation. The data of the remaining sections is presented in Appendix 1.

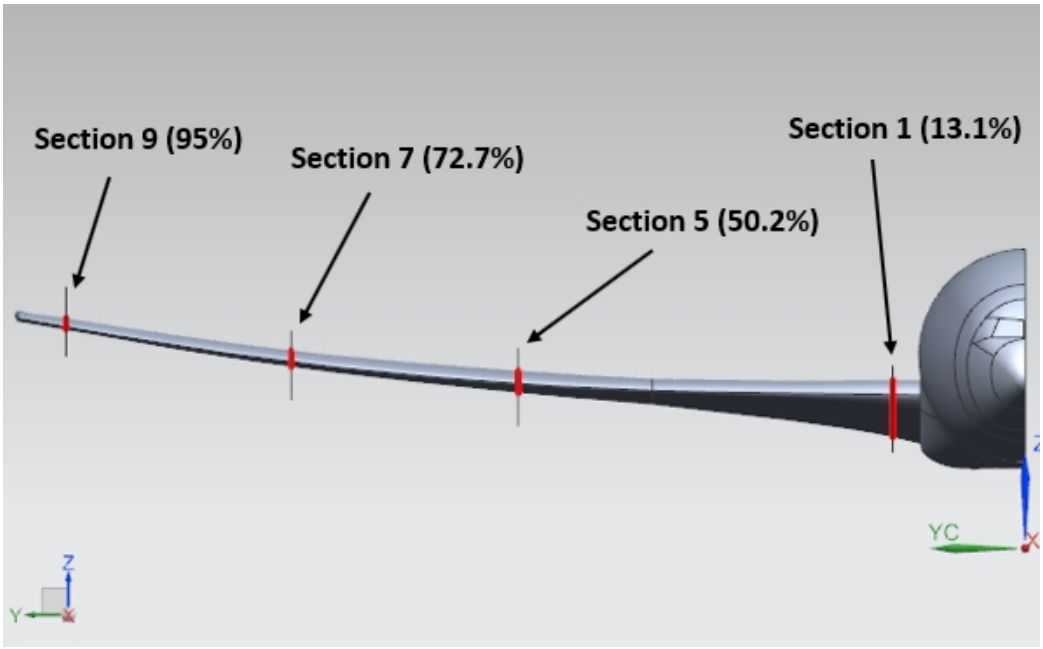

Figure 4-5. Wing sections for pressure coefficient measurement

The data from section 7 is presented on Figure 4-6, 4-7.

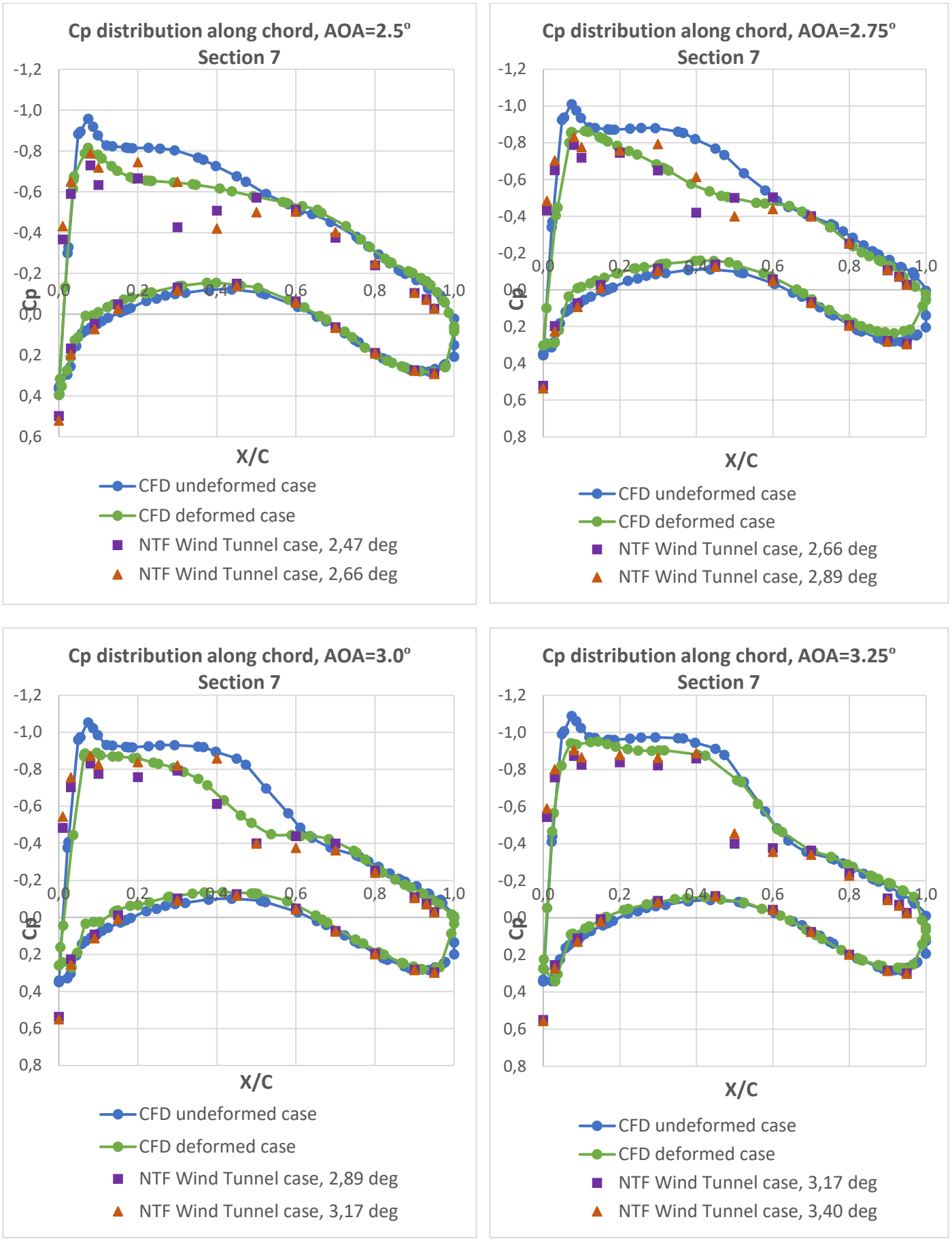

Figure 4-6. Pressure coefficient distribution, Section 7, AOA=2.5;3.25

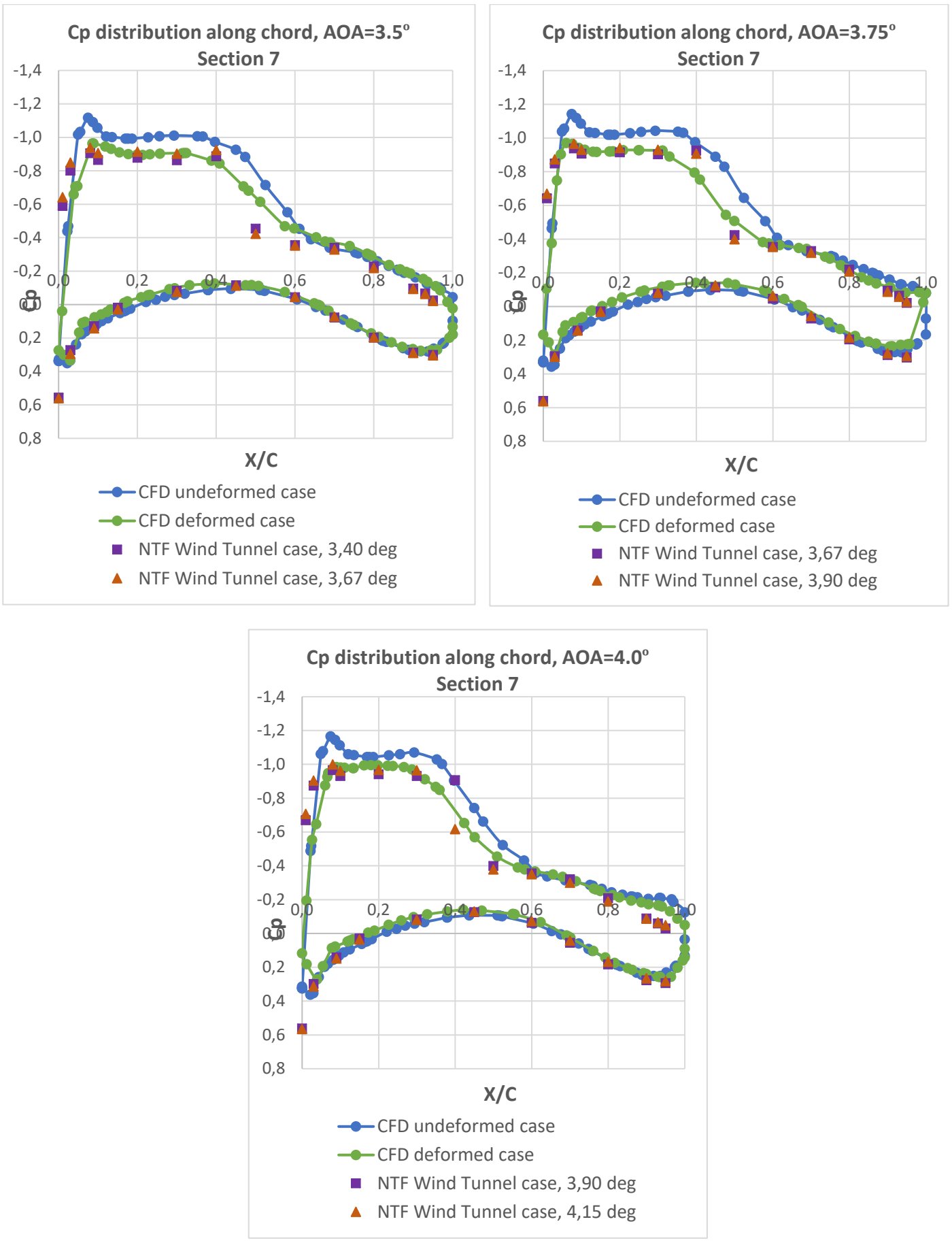

Figure 4-7. Pressure coefficient distribution, Section 7, AOA=3.5;4.0

The data from section 9 is presented on Figure 4-8, 4-9.

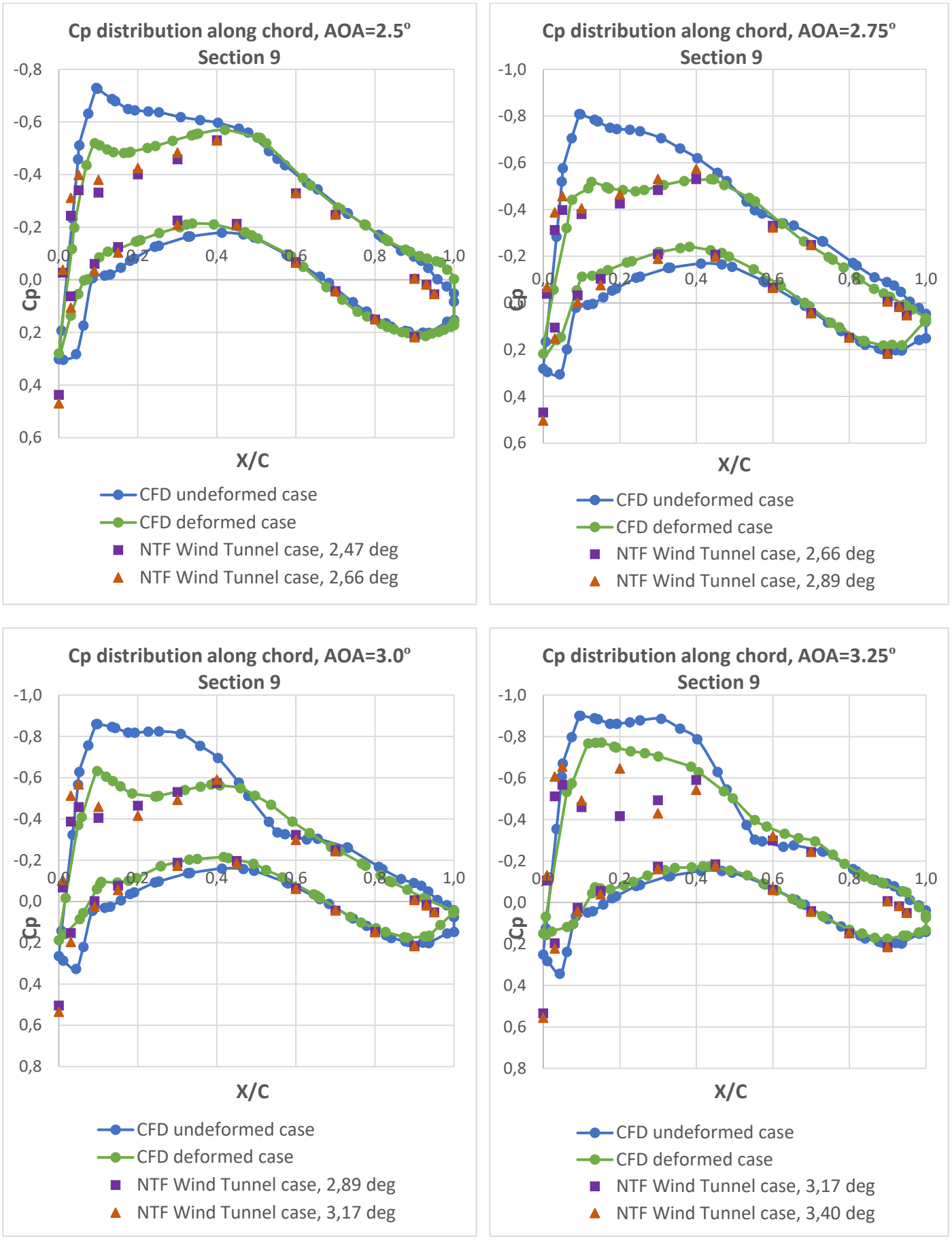

Figure 4-8. Pressure coefficient distribution, Section 9, AOA=2.5;3.25

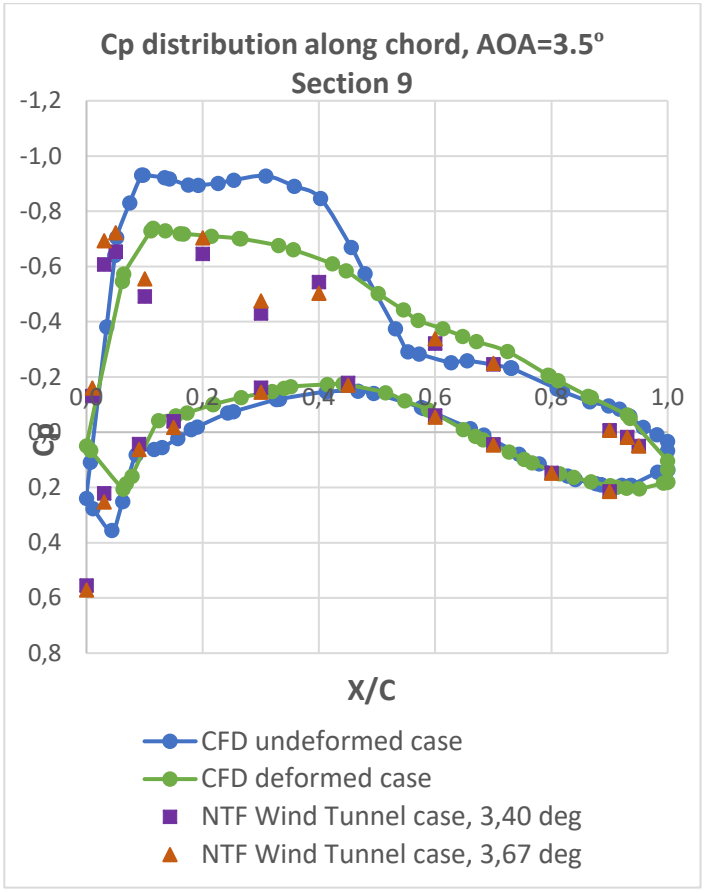

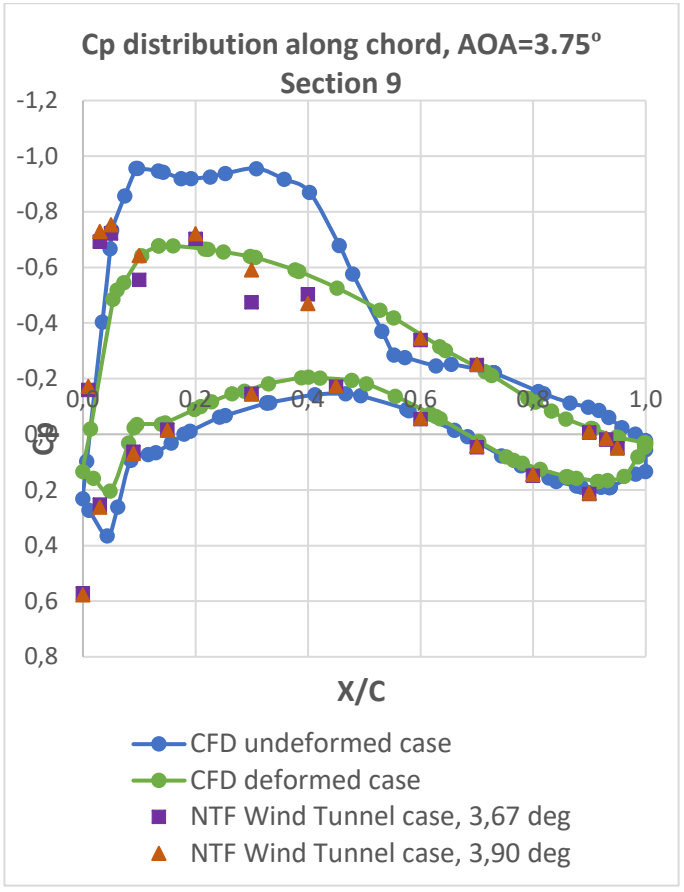

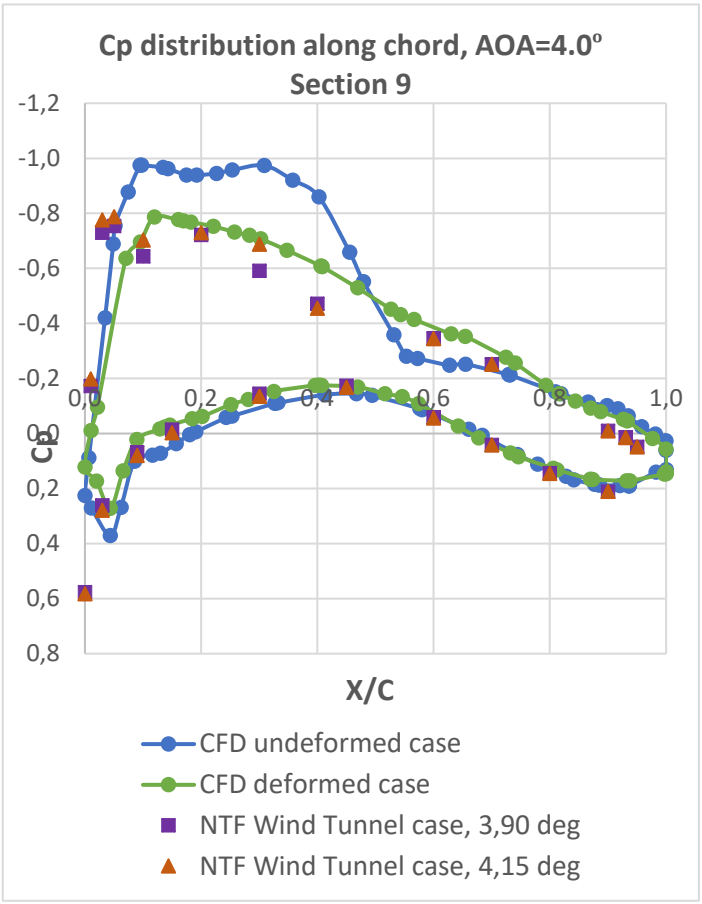

Figure 4-9. Pressure coefficient distribution, Section 9, AOA=3.5;4.0

The pressure coefficient decreases with the section being closer to the wingtip. This well agrees with the behavior of the non-infinite wing in the flow.

Generally, for deformed geometry the pressure coefficient values are smaller compared to undeformed case. It can be noted that the effect of deformation significantly decreases negative pressure drop, which has direct influence to the aerodynamic coefficients, mainly lift coefficient as it is dependent on the pressure the most. The negative pressure coefficient distribution along the wing is illustrated on the figure below (deformed case, AOA=3.75 º). For the clarity, the Mach number distribution along the surface of the aircraft is presented here as well.

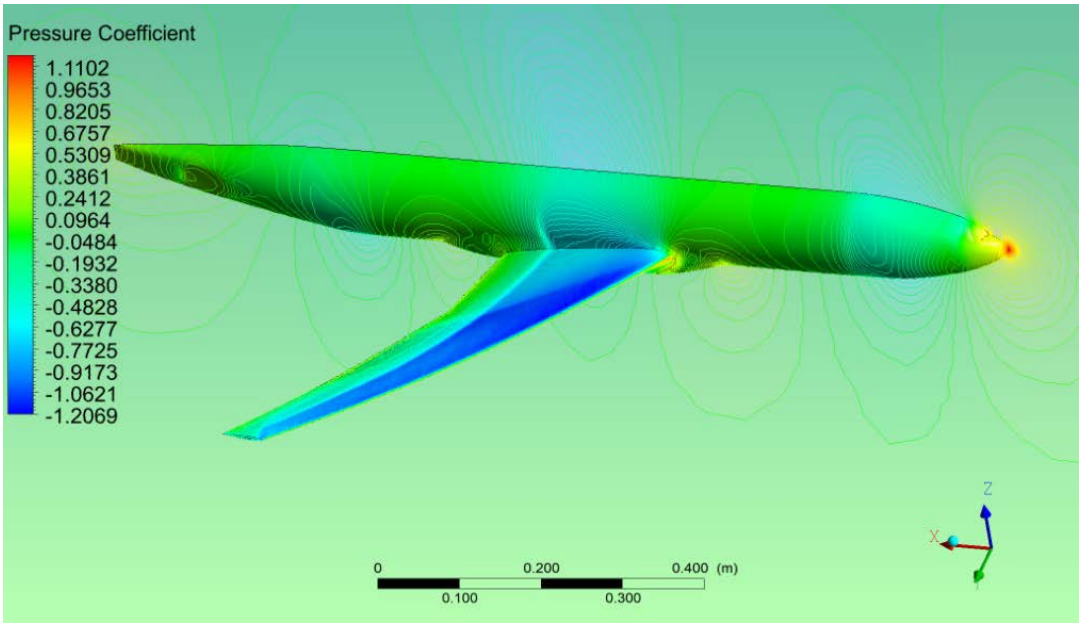

Figure 4-10. Pressure coefficient distribution along the surface of the aircraft model. Deformed case AOA=3.75 º

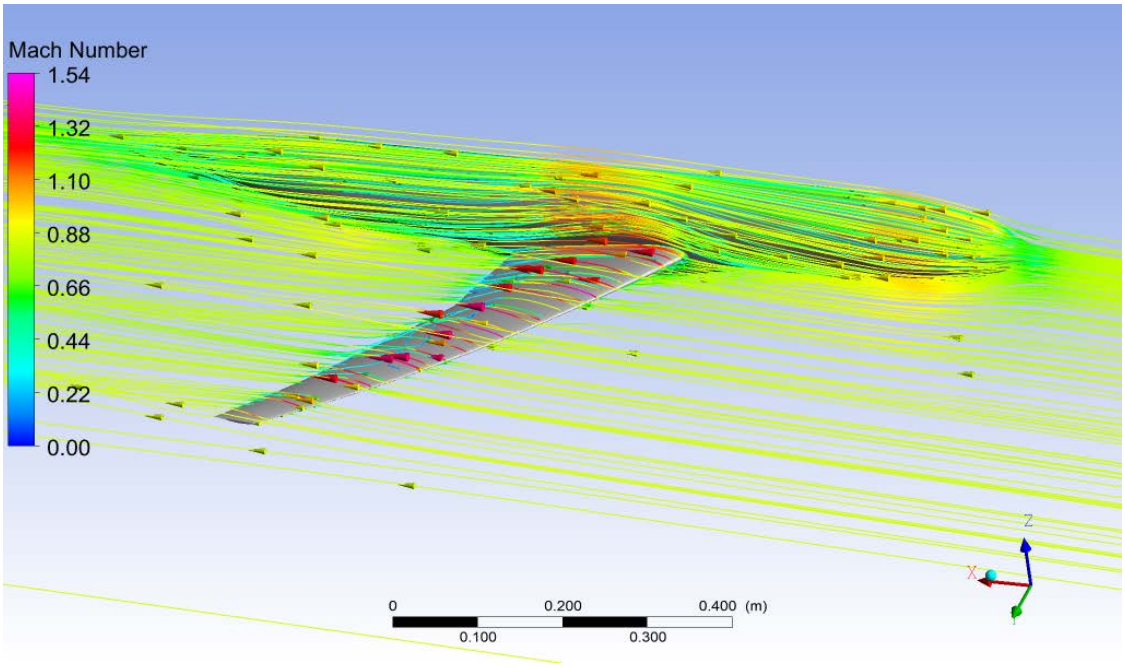

Figure 4-11. Mach number distribution along the surface of the aircraft model. Deformed case AOA=3.75 º

Also, at higher angles of attack, it is possible to notice the sudden change in pressure coefficient at mid-chord. This occurs due to the generation of the shock. The pressure drop has minimized behavior and it is located more aft, this happens because examined airfoil has supercritical design. It is possible to see, that effect of deformation has influence on the position of the shockwave generation along the chord. At the sections with significant sudden changes in pressure (Section 7 and 9), the flow separation regions occur due to this effect. For the clarity, next figures illustrate flow separation region in the vicinity of the shock wave (deformed case, AOA=3.75 º).

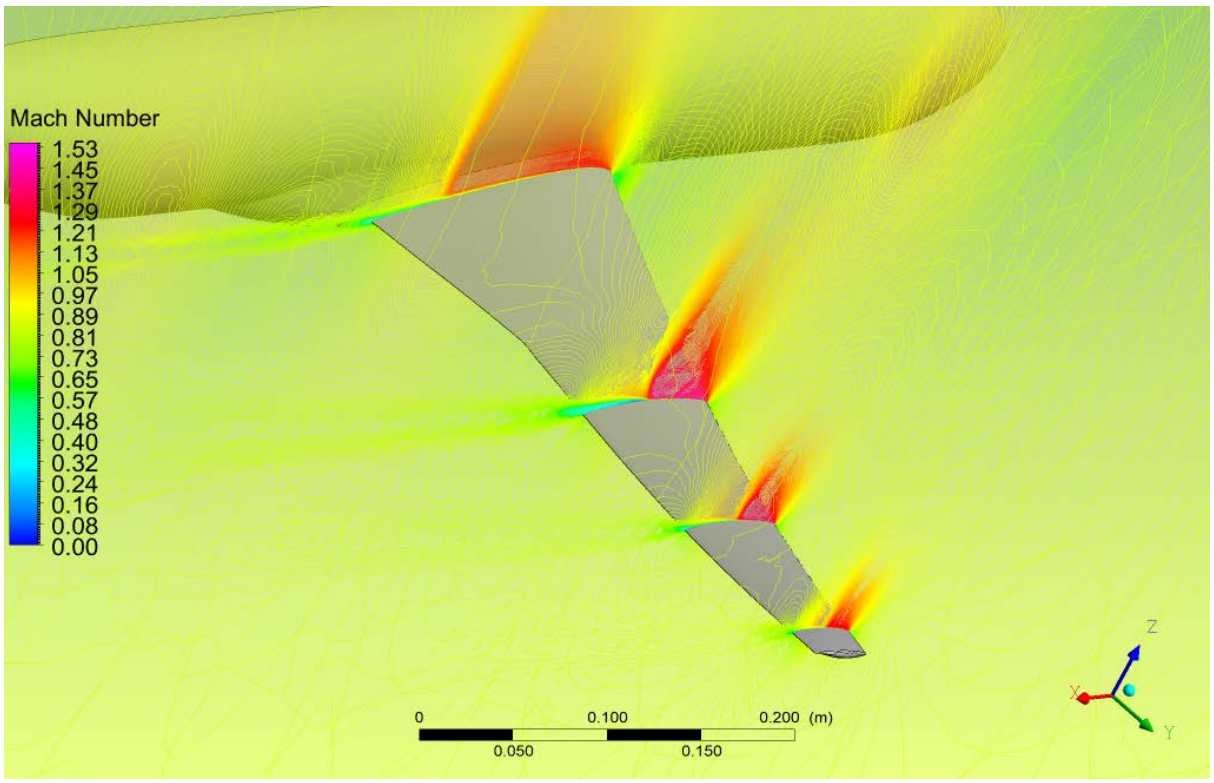

Figure 4-12. Mach number contours in Sections 1,5,7 and 9. Deformed case AOA=3.75 º

5. Conclusion

The effect of deformation on the aerodynamic characteristics of the aircraft model was studied using NASA CRM model. The analysis was performed based on the CFD simulation of two cases: un-deflected aircraft model geometry and the aircraft model geometry with deflections from aeroelastic effects for the different angles of attack. The CFD analysis was conducted using ANSYS Fluent software package, ANSYS Design Modeler and ANSYS Meshing were used for geometry modification and computational grid design respectively.

First the grid independence study was performed, several grids were designed in order to see grid influence on the computed results. During the grid independence study, it was shown that the grid with 3060448 elements is best fit for the given problem.

Next the turbulence study has been conducted, where computational performance of 4 different turbulence was examined, in order to see how turbulence modeling affects the results of the CFD computation. It was chosen to proceed with SST k-omega turbulence model for further computation as this model showed good accordance with experimental data and offered good stability and fast convergence of the solution during computation process.

The computation was performed for angle of attack 2.5-4º with 0.25º step for original un-deflected geometry and geometry with aeroelastic effect deflections accordingly. Flow conditions were specified according to NTF test conditions. Each case was running 200 iterations, which was enough for results to converge. To have more realistic picture, the obtained data was compared to the experimental results from NTF Wind tunnel.

As it follows from the obtained data, it is shown that the deformation effect decreases the lift coefficient by 10% on average and the drag coefficient by 13% on average. The pitching moment coefficient experiences a decrease by 16% due to the effect of deformation.

The pressure coefficient (Cp) distributions in defined cross sections along the wingspan were also examined. Section 1 corresponded to 13,1% of half-wingspan, Section 5 corresponded to 50,2% of half-wingspan, Section 7 lied in 72,7% of half-wingspan, Section 9 lied in 95% of half-wingspan. The results were compared to NTF Wind Tunnel data from corresponding wing section.

From the obtained data it was found that the values of the deformed model are generally smaller compared to the Cp distributions of the rigid model. The effect of deformation decreases the negative peaks of pressure which has direct influence on the aerodynamic coefficients. Therefore, it is possible to conclude that effect of deformation significantly influences the aerodynamic characteristics of the given aircraft model. The deformation effect decreases values of the aerodynamic coefficients, thus decreasing overall aerodynamic performance of the aircraft model.

Looking at results is important to mention difference between CFD data and NTF Wind Tunnel experimental data, mainly there is a notable difference in pitching moment coefficient prediction. The better agreement with experimental values could have been achieved by adding the supporting device of the model (sting) from the wind tunnel to the geometrical model and taking it into account during CFD analysis. Also, improvement in the results could have been achieved by taking into account the wind tunnel walls with adjusted boundary condition of perforated wall and improving mesh quality by switching to structured hexa mesh. Nevertheless, the obtained results are considered as reliable in the scope of this work.

6. References

[1] NASA. *NASA Common Research Model.* [Online] Available: https://commonresearchmodel.larc.nasa.gov/

[2] Vassberg, J.C., DeHaan, M.A., Rivers, S.M., and Wahls, R.A. (2008) *Development of a Common Research Model for Applied CFD Validation Studies*. AIAA Paper 2008-6919, AIAA Applied Aerodynamics Conference, Honolulu, USA

[3] Rivers, M. B. and Dittberner, A. (2011). *Experimental Investigations of the NASA Common Research Model in the NASA Langley National Transonic Facility and the NASA Ames 11-ft Transonic Wind Tunnel (Invited)*. AIAA Paper 2011-1126.

[4] Liu, T., Radeztsky, R., Garg, S., Cattafesta, L. (1999). *A Videogrammetric Model Deformation System and its Integration with Pressure Paint*. 7th AIAA Aerospace Sciences Meeting and Exhibit, AIAA 99-0568.

[5] Mouton, S. (2012). *Prediction of the Aerodynamic Effect of Model Deformation during Transonic Wind Tunnel Tests.* French Aerospace Lab.

[6] Anderson, J. D. *Fundamentals of Aerodynamics.* McGraw Hill. (Ed.). (2001).

[7] Keye, S., Rudnik, R. (2015). *Validation of Wing Deformation Simulations for the NASA CRM Model using Fluid-Structure Interaction Computations*. AIAA Paper 2015-0619.

[8] Jameson, A., Vassberg, J. (2001). *Computational Fluid Dynamics for Aerodynamic Design: Its Current and Future Impact*. 39th Aerospace Sciences Meeting and Exhibit Reno, NV, U.S.A.

[9] Anderson, J. D. (1995). *Computational fluid dynamics: the basics with applications*. New York: McGraw-Hill.

[10] Versteeg, H. & Malalasekera, W. (2007). *An introduction to computational fluid dynamics : the finite volume method*. Harlow, England New York: Pearson Education Ltd.

[11] Jameson, A. (2015). Computational Fluid Dynamics Past, Present and Future. Aerospace Computing Laboratory, Stanford University

[12] NASA. *Navier-Stokes Equations*. [Online] Available: https://www.grc.nasa.gov/www/k-12/airplane/nseqs.html

[13] ANSYS Inc. (2016). *ANSYS FLUENT 17.0 Theory Guide*.

[14] Davidson, L. (2003). *An introduction to turbulence models.* Chalmers university of technology, Getebörg, Sweden.

[15] Wilcox, D. (2006). *Turbulence modeling for CFD.* La Cãnada, Calif: DCW Industries.

[16] NASA. *AIAA CFD Drag Prediction Workshop*. [Online] Available: http://aaac.larc.nasa.gov/tsab/cfdlarc/aiaa-dpw/

[17] NASA. *Langley National Transonic Facility, Test 197*. [Online] Available: https://commonresearchmodel.larc.nasa.gov/experimental-approach/test-conditions/langley-national-transonic-facility/

[18] Siemens NX 10 [Computer software]. Copyright 2016-2018 Siemens PLM Software.

[19] ANSYS Design Modeler 17.2 [Computer software]. Copyright 2016-2018 ANSYS Inc.

[20] ANSYS Fluent 17.2 [Computer software]. Copyright 2016-2018 ANSYS Inc.

[21] ANSYS Meshing 17.2 [Computer software]. Copyright 2016-2018 ANSYS Inc.

[22] ANSYS CFD-Post 17.2 [Computer software]. Copyright 2016-2018 ANSYS Inc.

[23] LEAP CFD Team. (2013) *Estimating the First Cell Height for correct Y+*. [Online] Available: https://www.computationalfluiddynamics.com.au

[24] Kalitzin, G., Medic, G., Iaccarino, G., Durbin, P. (2004). *Near-wall behavior of RANS turbulence models and implications for wall functions.* Stanford University. Stanford, CA 94305-3030, USA

[25] Walters, D. K., Cokljat, D. (2008). *A three-equation eddy-viscosity model for Reynolds-averaged Navier-Stokes simulations of transitional flow.* Journal of Fluids Engineering. doi: 10.1115/1.2979230

7. Attachments

Attachment 1: Pressure coefficient distribution along the chord, Section 1

Attachment 2: Pressure coefficient distribution along the chord, Section 5

Attachment 3: Grid independent study: tables of values during convergence procedure [Excel file format]

Attachment 4: Turbulence model study: tables of values during convergence procedure [Excel file format]

Attachment 5: Fluent setup [XML file format]

Attachment 6: Tables of values of the pressure coefficient along the chord in examined wing sections [Excel file format]

Attachment 1

Section 1 (13,1% of half-wingspan)

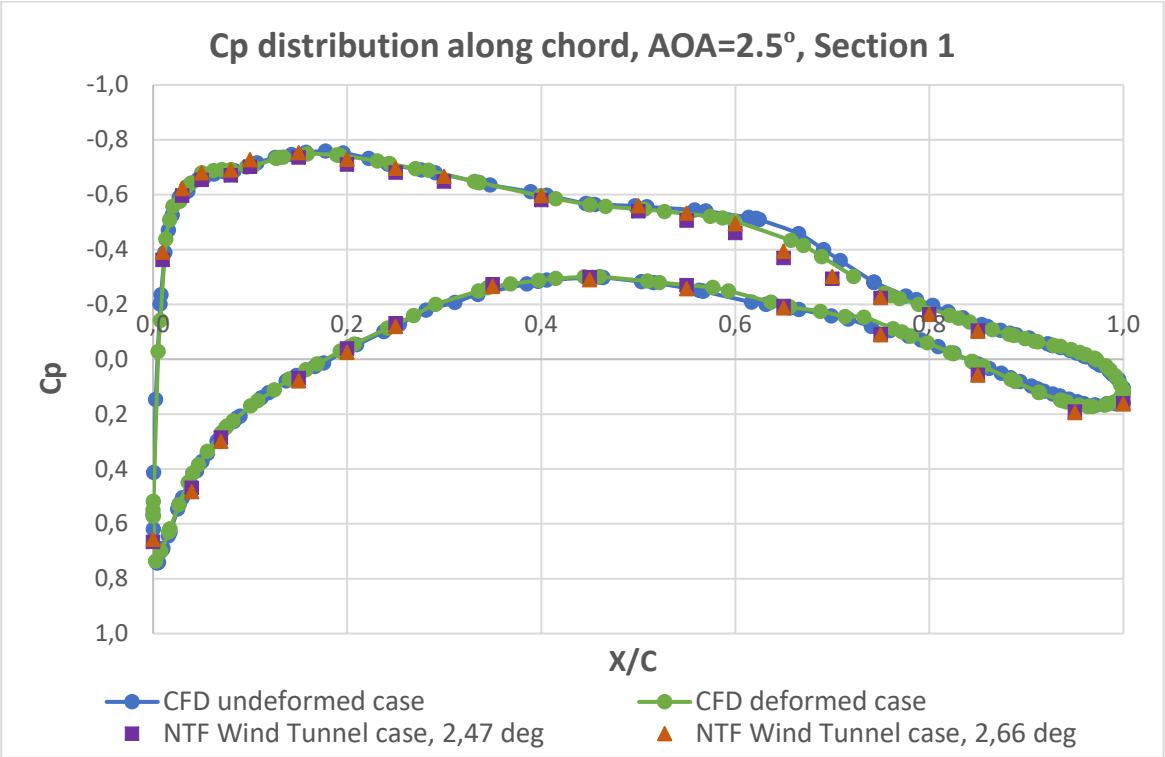

Attachment 1-1. Pressure coefficient distribution along the chord. AOA=2.5 deg, Section 1

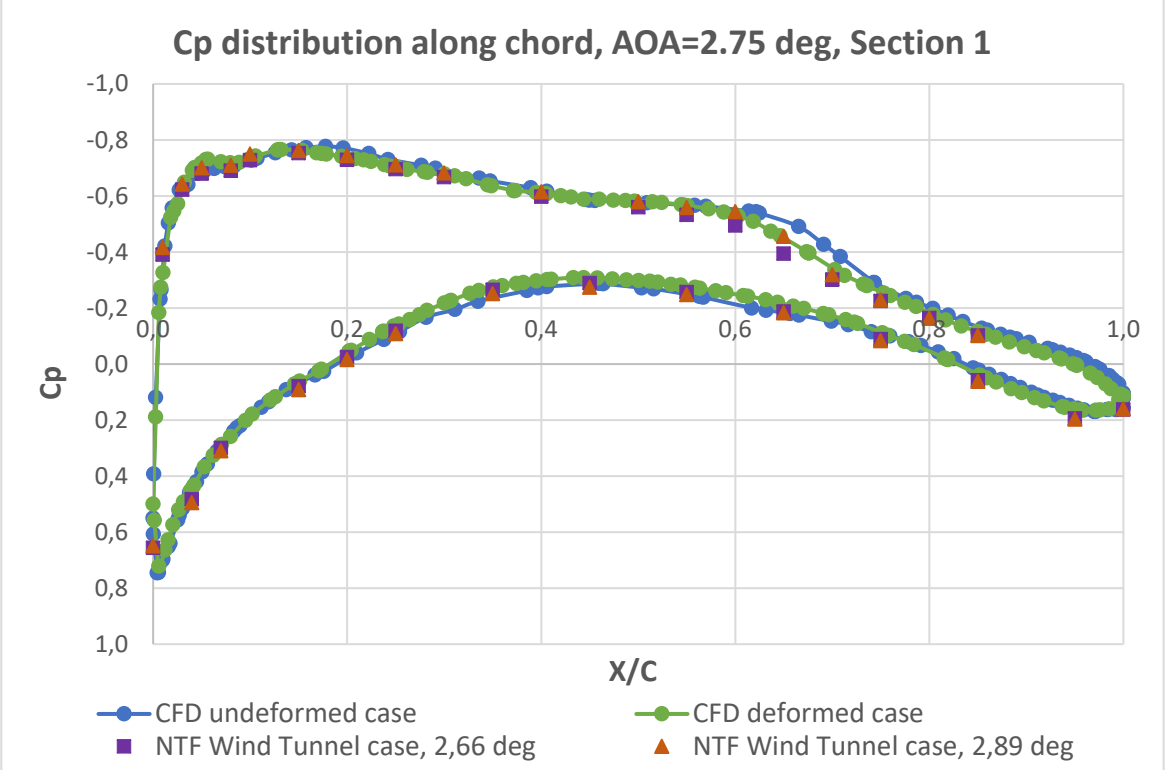

Attachment 1-2. Pressure coefficient distribution along the chord. AOA=2.75 deg, Section 1

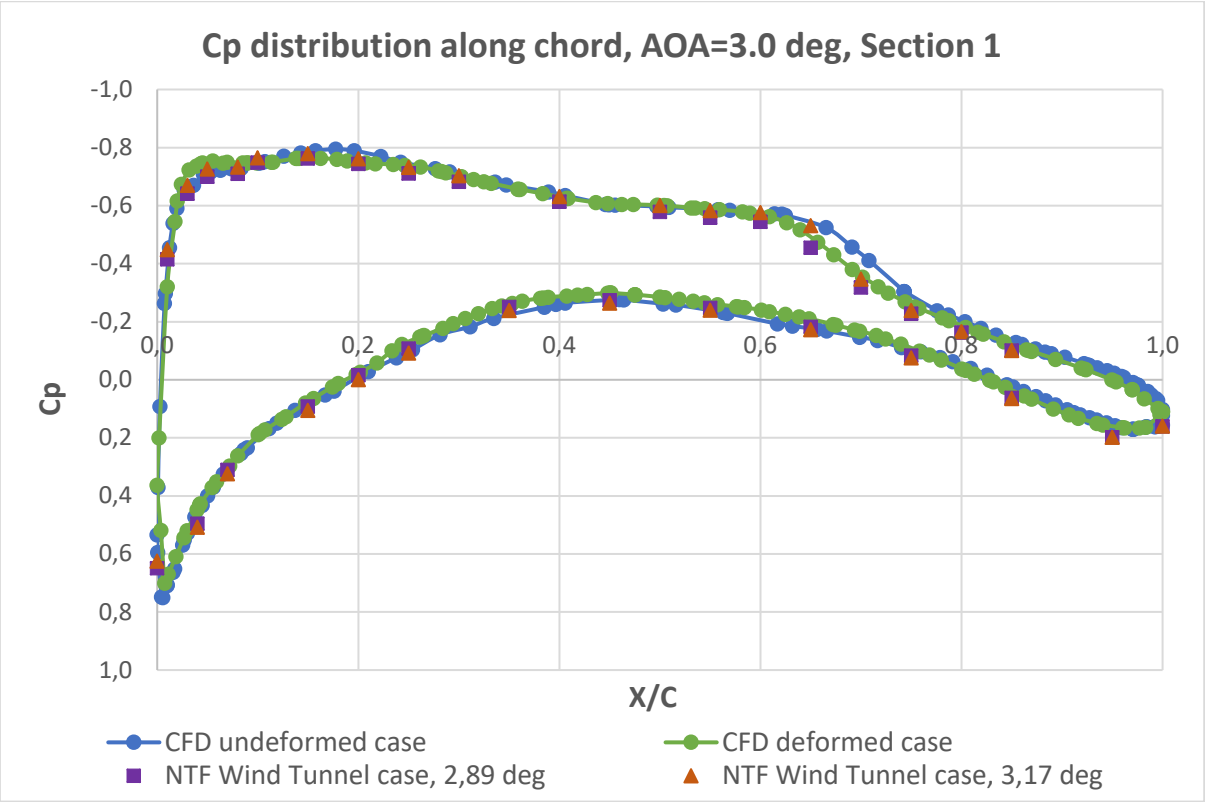

Attachment 1-3. Pressure coefficient distribution along the chord. AOA=3.0 deg, Section 1

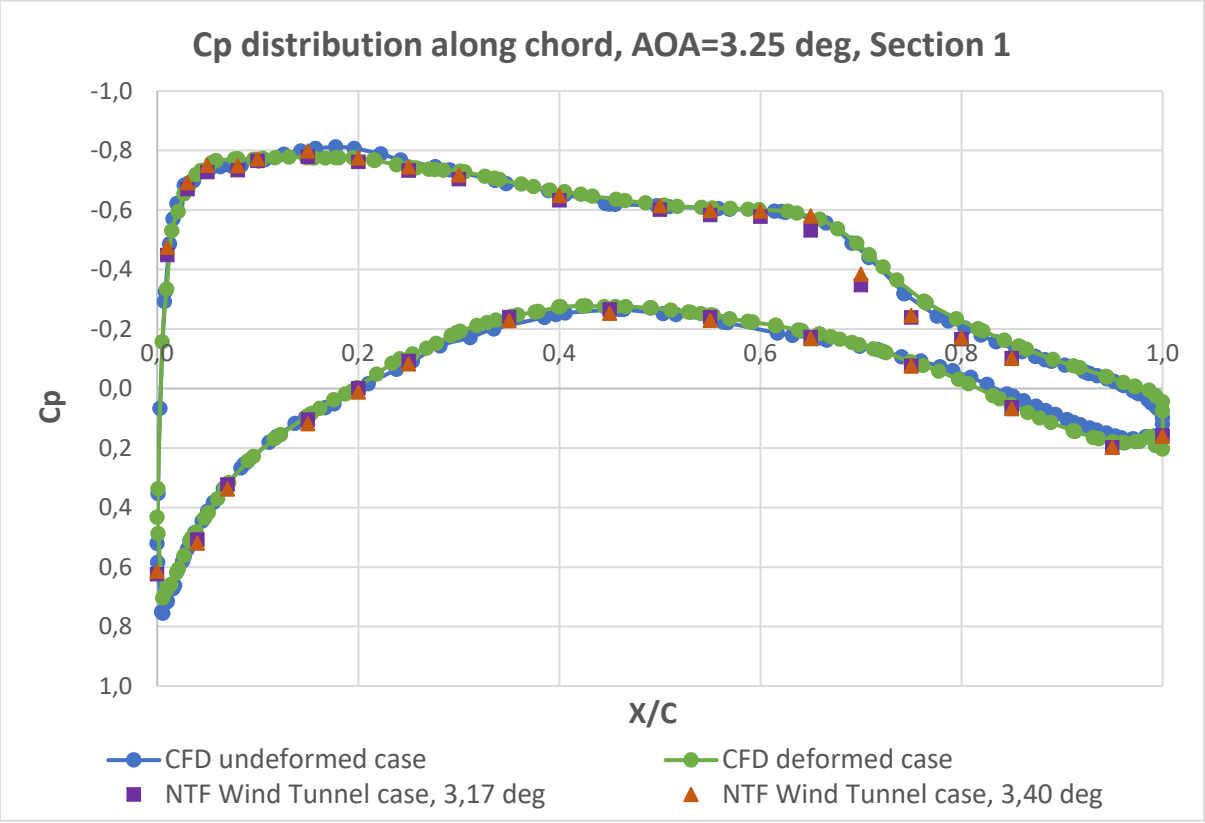

Attachment1-4. Pressure coefficient distribution along the chord. AOA=3.25 deg, Section 1

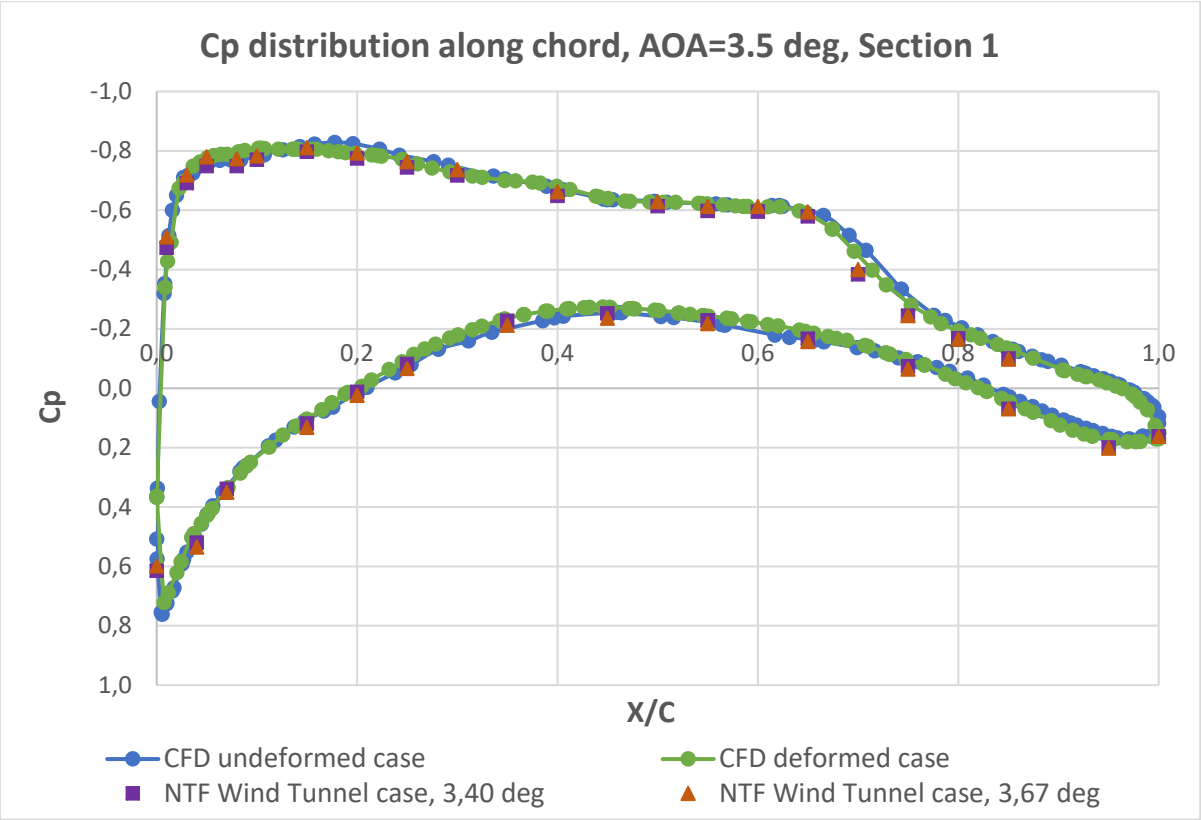

Attachment 1-5. Pressure coefficient distribution along the chord. AOA=3.5 deg, Section 1

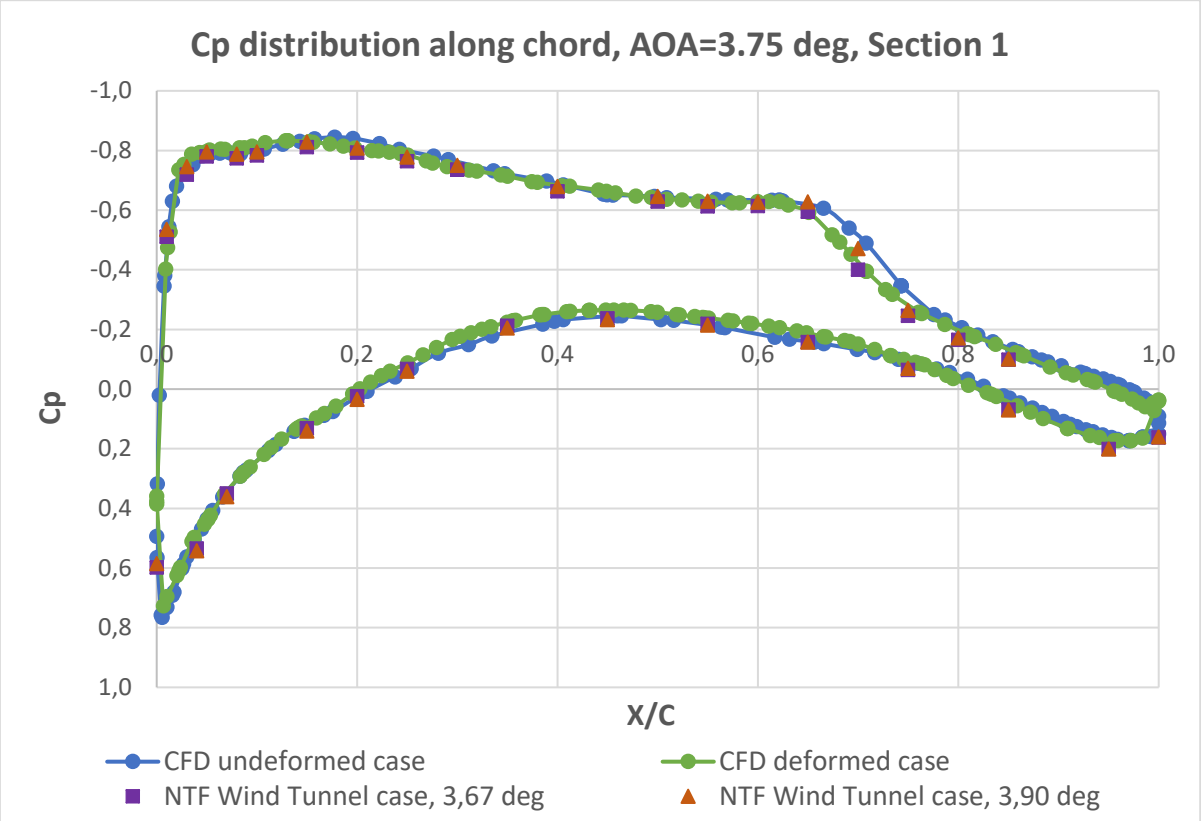

Attachment1-6. Pressure coefficient distribution along the chord. AOA=3.75 deg, Section 1

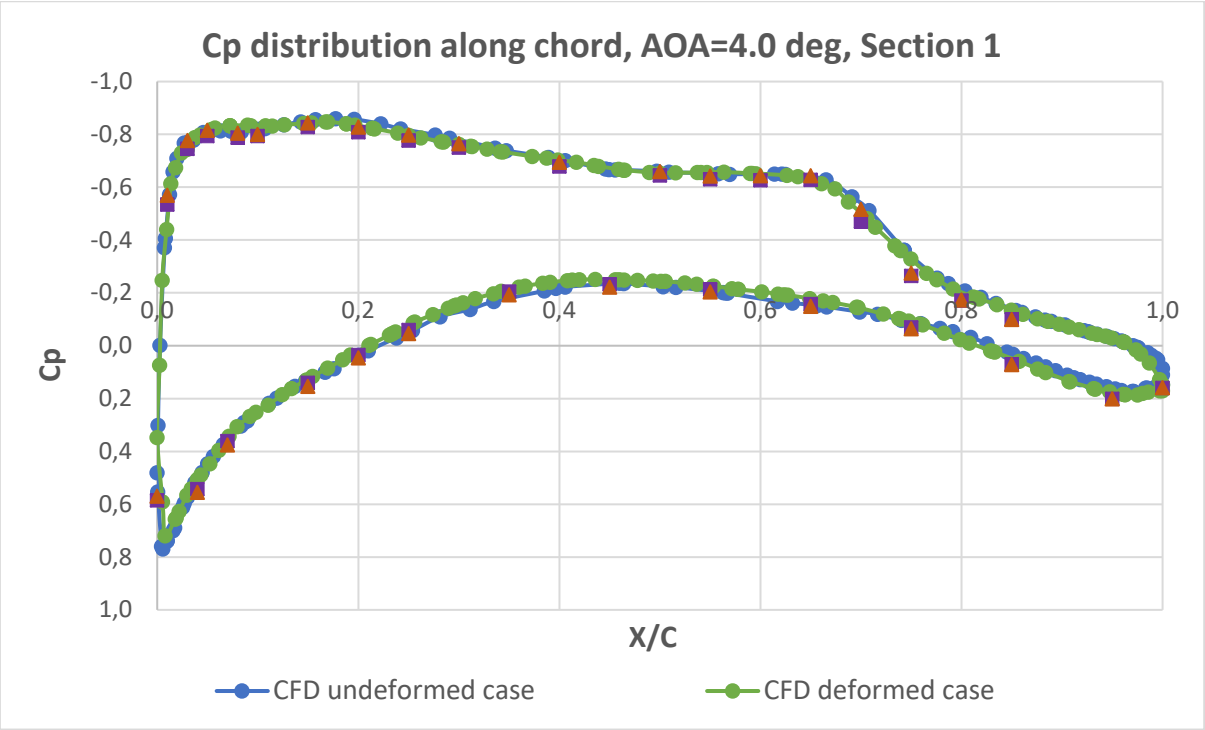

Attachment 1-7. Pressure coefficient distribution along the chord. AOA=4.0 deg, Section 1

Attachment 2

Section 5 (50,2% of half-wingspan)

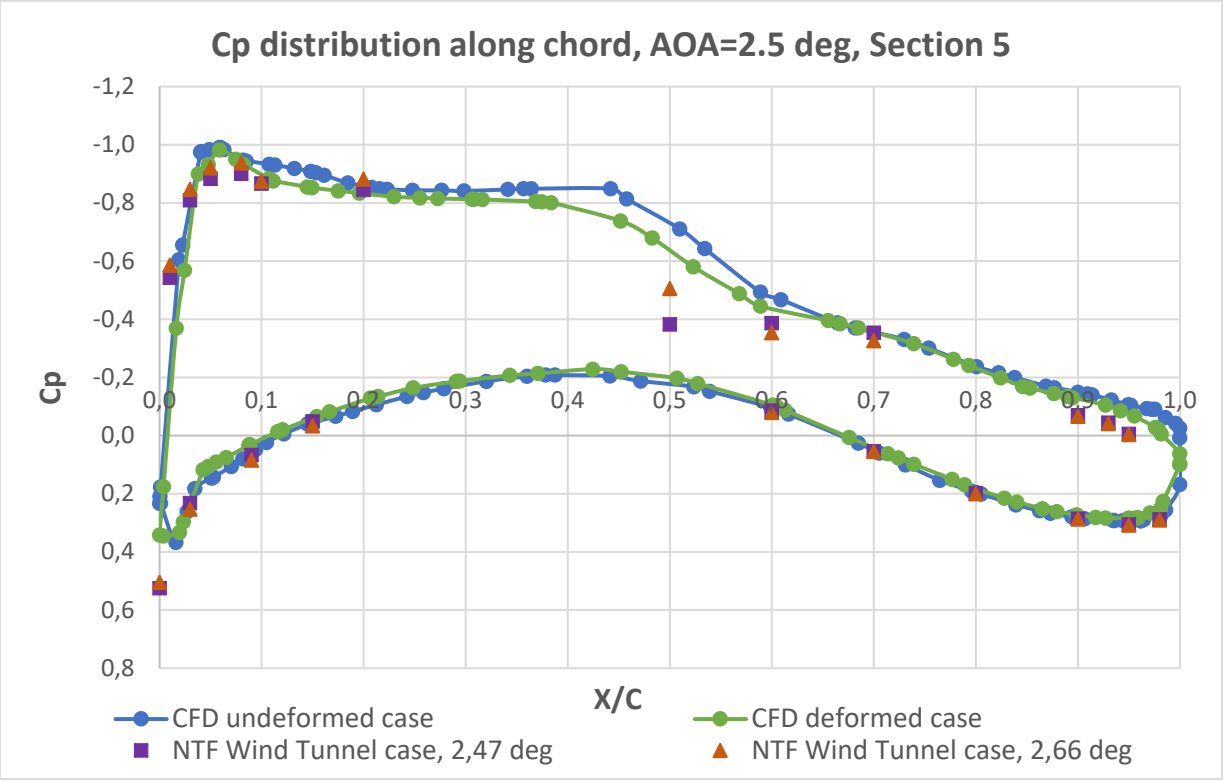

Attachment 2-1. Pressure coefficient distribution along the chord. AOA=2.5 deg, Section 5

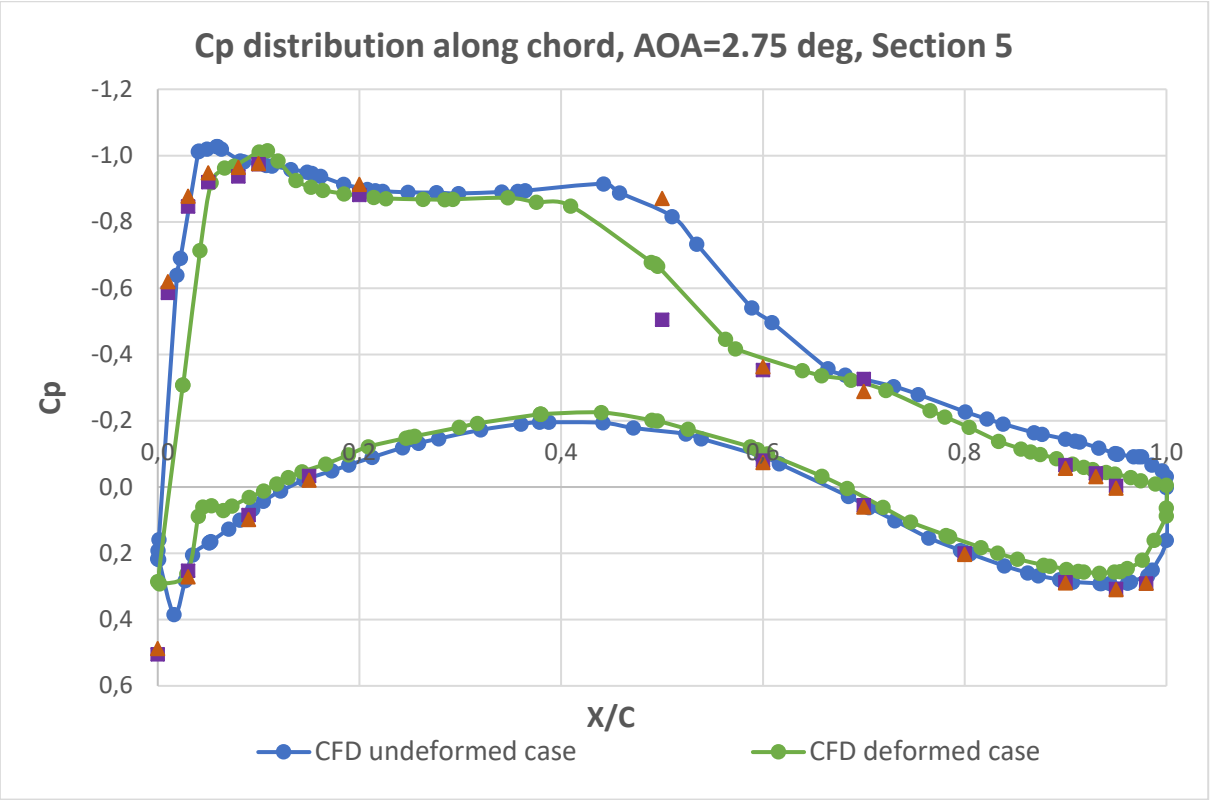

Attachment 2-2. Pressure coefficient distribution along the chord. AOA=2.75 deg, Section 5

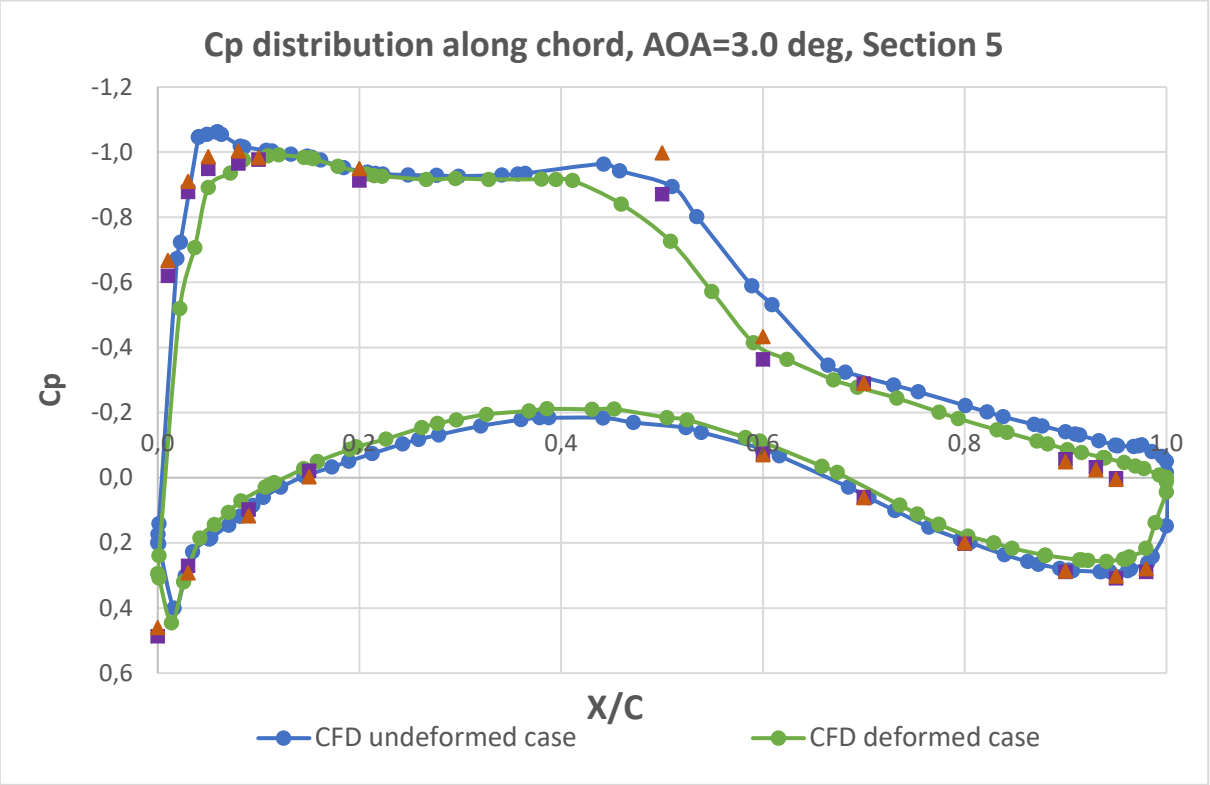

Attachment 2-3. Pressure coefficient distribution along the chord. AOA=3.0 deg, Section 5

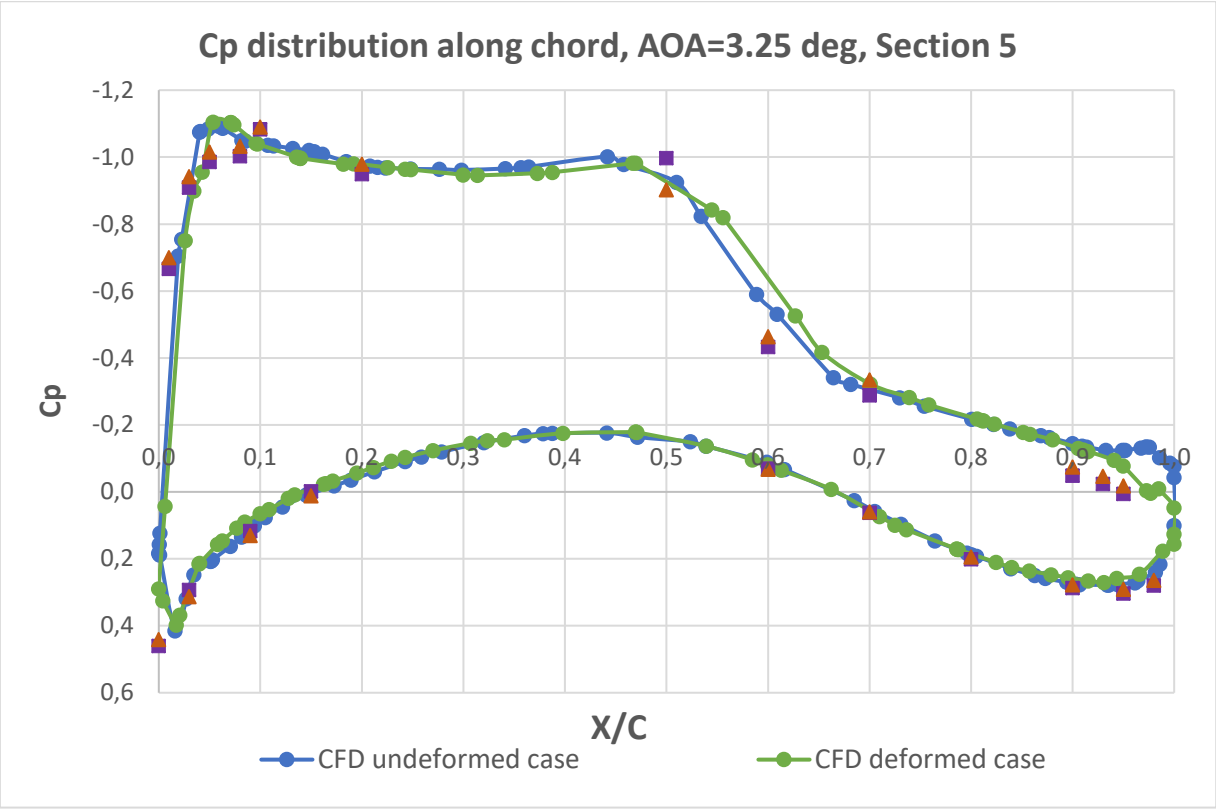

Attachment 2-4. Pressure coefficient distribution along the chord. AOA=3.25 deg, Section 5

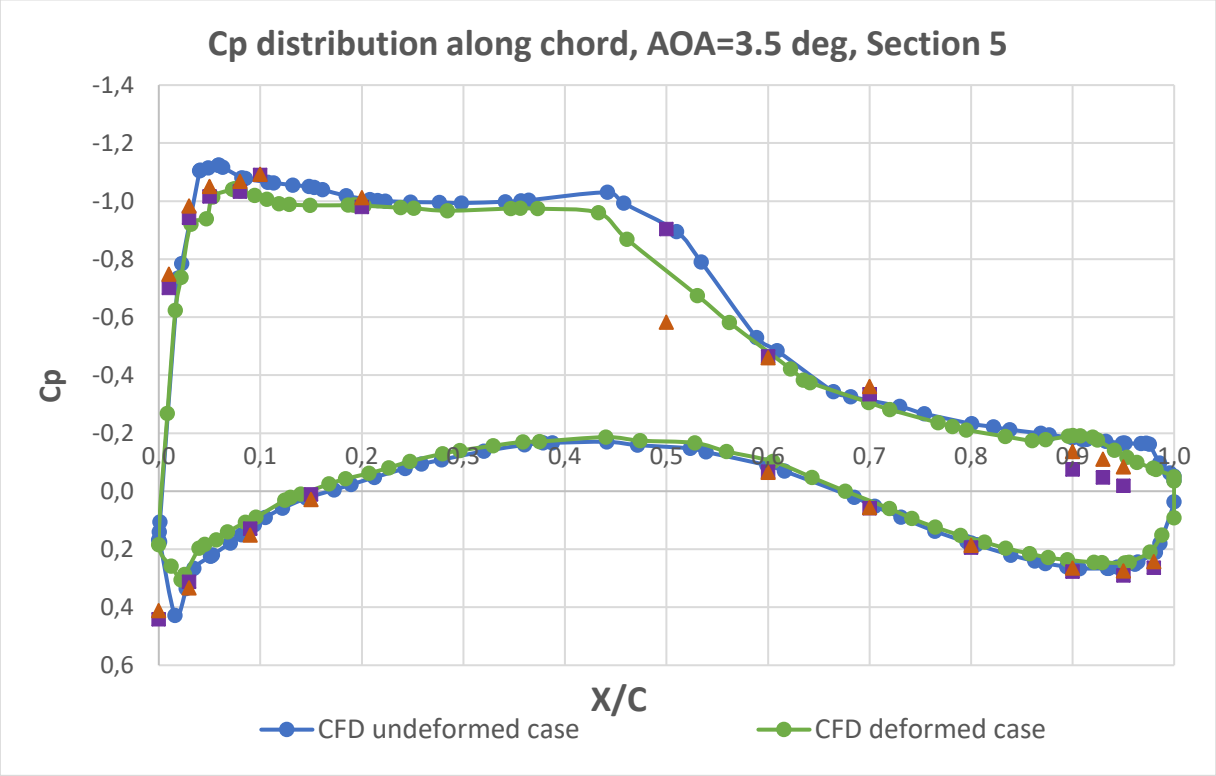

Attachment 2-5. Pressure coefficient distribution along the chord. AOA=3.5 deg, Section 5

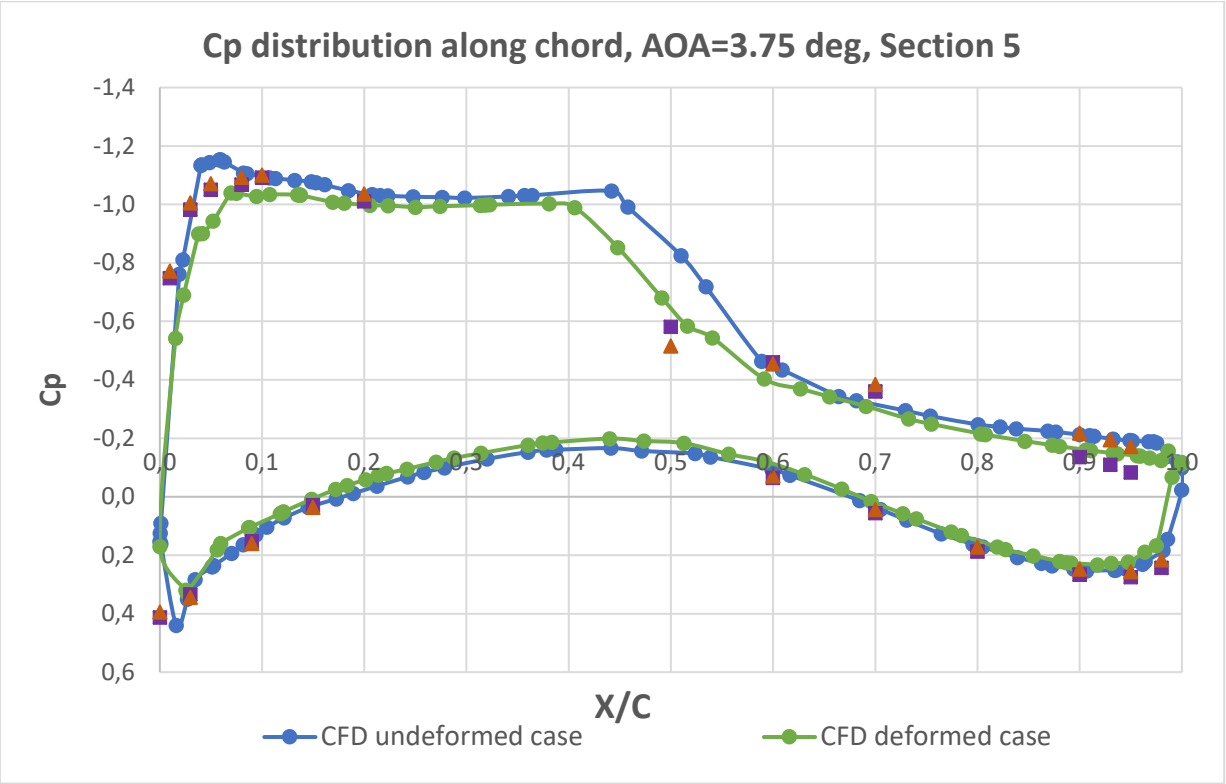

Attachment 2-6. Pressure coefficient distribution along the chord. AOA=3.75 deg, Section 5

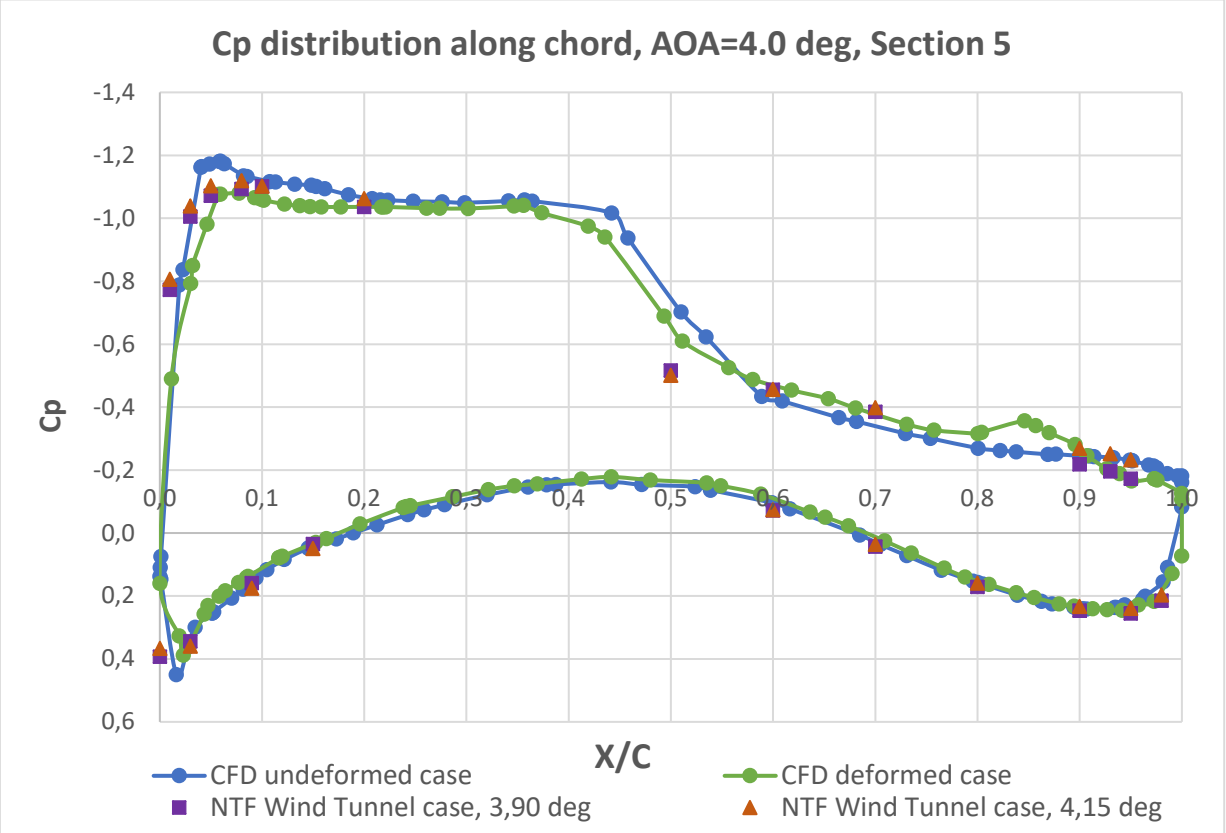

Attachment 2-7. Pressure coefficient distribution along the chord. AOA=4.0 deg, Section 5